Article

Developmental Cell

Global versus local matrix remodeling drives rotational versus invasive collective migration of epithelial cells

Graphical abstract

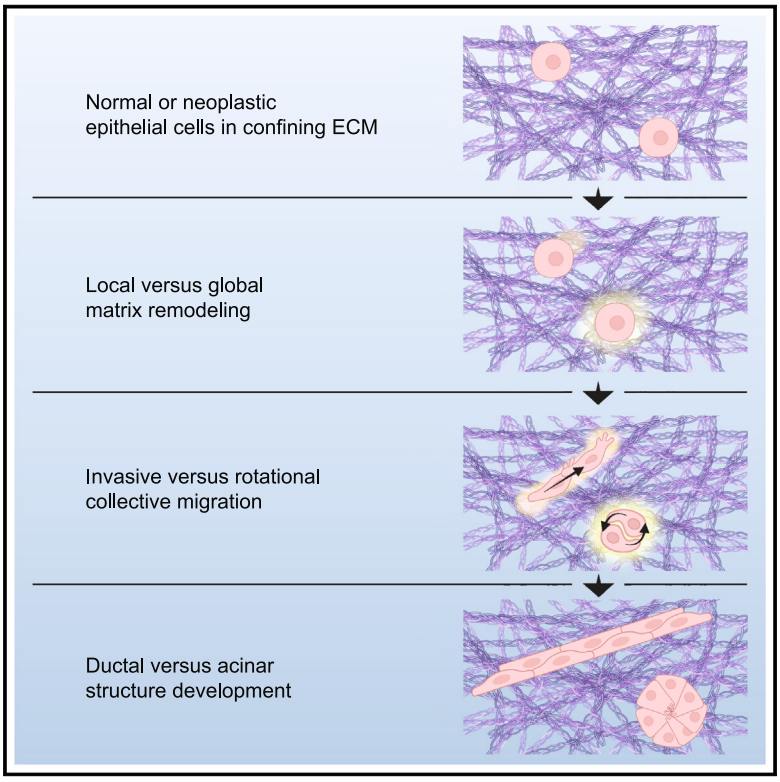

Authors

Sural K. Ranamukhaarachchi, Alyssa Walker, Man-Ho Tang, William D. Leineweber, Sophia Lam, Wouter-Jan Rappel, Stephanie I. Fraley

Correspondence

wouter@ucsd.edu (W.-J.R.), sifraley@ucsd.edu (S.I.F.)

In brief

Ranamukhaarachchi et al. find that rotational and invasive collective migrations arise in confining 3D environments, regardless of whether cells express cadherins. Local matrix remodeling by MMPs initiates invasive collective migration, whereas rotational collective migration is MMP independent and associated with ITGβ1-mediated matrix remodeling that is localized globally around the cell body.

Highlights

- Localization and type of matrix remodeling regulate collective migration behaviors
- Rotational collective migration utilizes global ITGβ1-mediated matrix remodeling
- Invasive collective migration depends on local MMP-mediated remodeling
- Rotational collective migration does not require cadherin-based cell-cell adhesion

Ranamukhaarachchi et al., 2025, Developmental Cell *60*, 1–14
March 24, 2025 © 2024 The Author(s). Published by Elsevier Inc.
https://doi.org/10.1016/j.devcel.2024.11.021

CellPress

Please cite this article in press as: Ranamukhaarachchi et al., Global versus local matrix remodeling drives rotational versus invasive collective migration of epithelial cells, Developmental Cell (2024), https://doi.org/10.1016/j.devcel.2024.11.021

Developmental Cell

CellPress
OPEN ACCESS

Article

Global versus local matrix remodeling drives rotational versus invasive collective migration of epithelial cells

Sural K. Ranamukhaarachchi,[1] Alyssa Walker,[1,3] Man-Ho Tang,[2,3] William D. Leineweber,[1] Sophia Lam,[1] Wouter-Jan Rappel,[2,*] and Stephanie I. Fraley[1,4,*]

[1]Department of Bioengineering, University of California, San Diego, La Jolla, CA 92093, USA
[2]Department of Physics, University of California, San Diego, La Jolla, CA 92093, USA
[3]These authors contributed equally
[4]Lead contact
*Correspondence: wouter@ucsd.edu (W.-J.R.), sifraley@ucsd.edu (S.I.F.)
https://doi.org/10.1016/j.devcel.2024.11.021

SUMMARY

The coordinated movement of cell collectives is essential for normal epithelial tissue development, maintenance, and cancer progression. Here, we report on a minimal 3D extracellular matrix (ECM) system wherein both invasive collective migration (ICM) and rotational collective migration (RCM) arise spontaneously from individually seeded epithelial cells of mammary and hepatic origin, regardless of whether they express adherens junctions, and lead to ductal-like and acinar-like structures, respectively. Quantitative microscopy and cellular Potts modeling reveal that initial differences in cell protrusion dynamics and matrix-remodeling localization generate RCM and ICM behavior in confining 3D ECM. Matrix-remodeling activity by matrix metalloproteinases (MMPs) is localized to the base of protrusions in cells that initiate ICM, whereas RCM does not require MMPs and is associated with ITGβ1-mediated remodeling localized globally around the cell body. Further analysis *in vitro* and *in vivo* supports the concept that distinct matrix-remodeling strategies encode collective migration behaviors and tissue structure.

INTRODUCTION

Exocrine organs, such as the mammary, salivary, and digestive glands, are composed of suprastructural networks of terminal acini connected to secretory ducts. During glandular morphogenesis, epithelial cells undergo collective migration to develop these core tissue subunits, which are described according to their shapes, ranging from spherical acinus structures to cylindrical ductal structures. Specific collective migration behaviors give rise to these distinct shapes: acini are developed by a persistent coordination of rotational movement, whereas ducts are developed by invasive collective movements, such as sprouting or branching.[1–3] Furthermore, morphogenic processes such as lactation and involution of the mammary gland require rapid transformations between these cylindrical ducts and spherical acinus structures, which require epithelial cells to switch between modes of invasive (invasive collective migration [ICM]) and rotational collective migration (RCM), respectively[4,5] (Figure 1A). Similar transformations are conserved in developmental programs such as *Drosophila* egg tissue elongation, where switching from RCM to ICM is a part of normal maturation.[6–9] Neoplastic epithelial cells can also mimic and aberrantly activate collective migration programs during cancer progression. A prominent manifestation is the hijacking of ICM by neoplastic cells, which can result in relatively normal-appearing epithelial duct architectures with or without expression of cell-cell adherens junctions.[3] RCM has not been observed in neoplastic epithelial cells, which has been attributed to their loss of E-cadherin-based adherens junctions.[1,2] Yet, microglandular adenomas and acinar cell carcinomas of the breast, salivary gland, and pancreas are characterized by a spherical morphology, wherein cancer cells arrange radially around a central lumen and exhibit indolent clinical behavior, which suggests that it is conceivable and possibly favorable for neoplastic cells to undergo RCM.[10–12] Along these lines, we previously observed that within a population of triple-negative breast cancer cells, some cells are capable of forming structures resembling rounded acinus-like morphologies, and others form elongated ductal-like morphologies when seeded in confining, high-density collagen type I.[13–17]

While collective movements are diverse and complex, their emergence is thought to arise from the interplay of cell-cell and cell-matrix interactions that is dependent on the position of cells within the collective, as well as the constraints imposed on the cells by the extracellular environment. Our current understanding emphasizes that ICM and RCM programs are initiated by establishing a collective front-rear polarity through coordination of the actin cytoskeleton.[7,18,19] RCM in normal epithelial

This is an open access article under the CC BY license (http://creativecommons.org/licenses/by/4.0/).

Please cite this article in press as: Ranamukhaarachchi et al., Global versus local matrix remodeling drives rotational versus invasive collective migration of epithelial cells, Developmental Cell (2024), https://doi.org/10.1016/j.devcel.2024.11.021

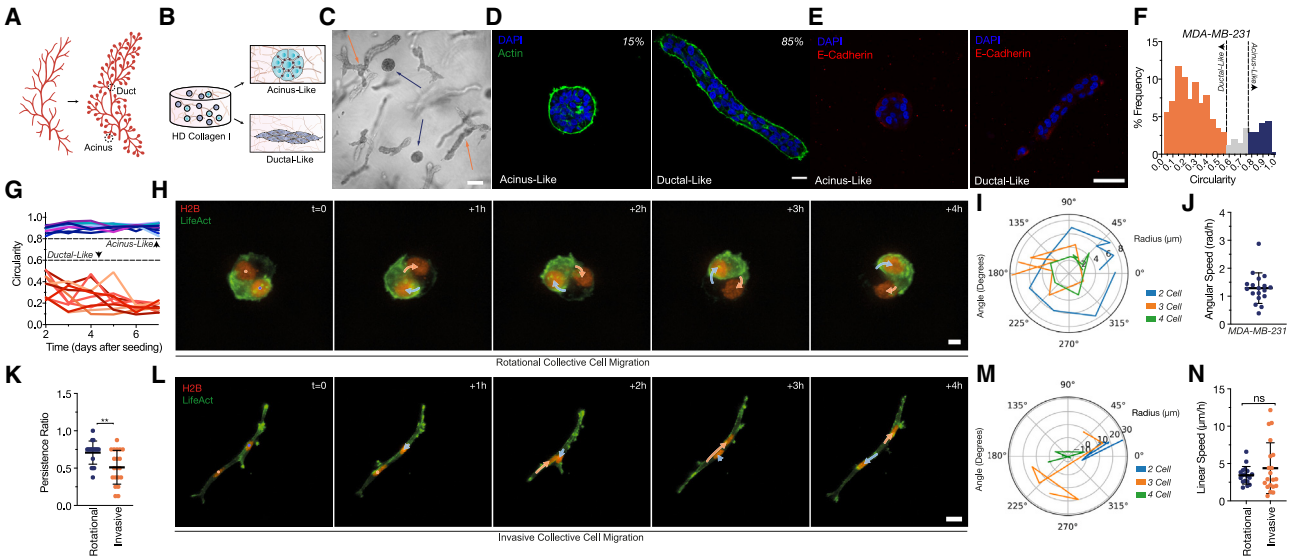

Figure 1. RCM and ICM emerge in confining ECM

(A) Cross-sectional schematic of mammary gland development. Created with BioRender.com.

(B) Cells seeded sparsely as single cells in high-density collagen type I (6 mg mL^{-1}) form clonal structures resembling either elongated ductal-like structures or rounded acinus-like structures over the course of 7 days.

(C) Bright-field images taken 7 days after seeding. Orange arrows indicate ductal-like structures, and blue arrows indicate acinus-like structures. Scale bar, 100 μm.

(D) Actin cytoskeleton substructure labeled in green and nuclei labeled in blue in acinus-like and ductal-like structures. Scale bar, 25 μm.

(E) E-cadherin expression in MDA-MB-231 in either acinus-like or ductal-like structures. Scale bar, 50 μm.

(F) Frequencies of ductal-like and acinus-like morphologies at 7 days in MDA-MB-231 cell lines. A circularity threshold of <0.6 for ductal-like phenotypes and >0.8 for acinus-like phenotypes was applied at 7 days (n = 342 multicellular structures).

(G) Cell cluster circularity from days 2 to 7 after seeding. A circularity threshold of <0.6 for ductal-like phenotypes and >0.8 for acinus-like phenotypes is sufficient to distinguish these phenotypes at early time points (n = 10 acinus-like structures and n = 10 ductal-like structures).

(H) Time-lapse images of circular 2-cell clusters of MDA-MB-231 cells undergoing persistent active rotations. Scale bar, 7 μm.

(I) Polar plot of example trajectories of rotational migration that persists for cells in 2-, 3-, and 4-cell clusters.

(J) Angular speed per cellular track of rotational MDA-MB-231 cells in 2-cell clusters (n = 18 individual cells, n = 9 cell clusters).

(K) Cell persistence ratio per cellular track for MDA-MB-231 rotational (n = 9 cell clusters) and invasive 2-cell clusters (n = 10 cell clusters).

(L) Time-lapse images of elongated 2-cell clusters of MDA-MB-231 cells undergoing collective invasion. Scale bar, 20 μm.

(M) Polar plot of example trajectories of invasive migration that persists for cells in 2-, 3-, and 4-cell clusters.

(N) Rectilinear speed per cellular track of invasive and rotational MDA-MB-231 cells in 2-cell clusters (n = 20 individual cells, n = 10 cell clusters). All error bars represent standard deviation from the mean.

Statistical significance is indicated as ns, not significant, (*) $p \leq 0.05$, (**) $p \leq 0.01$, (***) $p \leq 0.001$, and (****) $p \leq 0.0001$.

cells requires strong intercellular cadherin junctions for polarity and movement initiation, while ICM can be orchestrated by polarized cells of higher junctional fluidity.[18,20] Collective movements also respond to contractile stresses from the matrix. Invasive ductal cells seeded in 3D collagen I sense and reinforce anisotropic stress from the extracellular matrix (ECM) during elongation but will initiate rotational migration to establish terminal acini when tension anisotropy is decreased due to gel detachment.[5] Movement within a physically confining ECM also requires active transformation of the surrounding matrix through proteolytic degradation or physical disruption. Proteolytic remodeling, specifically, has been well-studied in the context of ICM, where cells generate macroscopic holes in the matrix by proteolytic removal using matrix metalloproteinases (MMPs), like membrane type 1-MMP (MT1-MMP/MMP-14).[21] Physical remodeling, which occurs through the bundling or breakage of the matrix, has been observed in protease-independent, collectively invasive, and rotational cells, but whether it plays a direct role in shaping the core glandular subunits remains largely undefined.[5,22] In this study, we use computational modeling and experiments to determine how cell-cell and cell-matrix interactions converge to direct ductal versus acinus morphogenesis in both normal and neoplastic epithelial cells.

RESULTS

RCM and ICM emerge in confining ECM

Neoplastic MDA-MB-231 cells seeded sparsely as single cells in high-density collagen type I (6 mg mL^{-1}) form clonal structures resembling either cylindrical duct-like structures or spherical acinus-like structures over the course of 7 days (Figures 1B–1D).[13–17] We first explored whether ICM and RCM behaviors contributed to the formation of these two structure types. RCM of MDA-MB-231 cells would be particularly surprising given that they do not express junctional E-cadherin (Figure 1E), and previous work has suggested an inability for neoplastic cells to undergo collective coherent angular rotations due to an absence of E-cadherin junctions.[1,2,5,18,23] To link the structures formed at

Please cite this article in press as: Ranamukhaarachchi et al., Global versus local matrix remodeling drives rotational versus invasive collective migration of epithelial cells, Developmental Cell (2024), https://doi.org/10.1016/j.devcel.2024.11.021

CellPress
OPEN ACCESS

7 days to early cell migration behaviors, we imaged cells after ~1 cell division cycle from day 2 through day 7 and quantified differences in cluster circularity. By applying a circularity threshold of <0.6 for ductal-like phenotypes and >0.8 for acinus-like phenotypes, we found that we could distinguish the phenotypes as early as ~36 h based on cellular shapes (Figure 1F). Elongated cells remained elongated, and circular cells remained circular as cells divided and structures formed (Figure 1G).

In cell lines stably expressing GFP-tagged LifeAct (to visualize the actin cytoskeleton) and mCherry-tagged H2B (to visualize nuclei), we tracked circular and elongated cells every hour for 10 h at the 2-cell stage. Live imaging of circular MDA-MB-231 cells revealed rotations in ~80%. Rotations persisted as cells divided and entered 3- and 4- cell clusters (Figures 1H–1J; Video S1). These cells did not exhibit a directional bias and occasionally switched chirality. To exclude the possibility that rotational cells were simply undergoing directionless oscillations, we measured the migration coherence using a previously established cell persistence ratio.[18] This metric quantified the proportion of time that cells migrated consistently in a clockwise (CW) or counterclockwise (CCW) radial direction such that a value of 0 or 1 indicated no directionality or completely CW/CCW, respectively. This analysis confirmed that rotational cells migrated coherently (Figure 1K). On the other hand, elongated cells collectively invaded, which continued through the 3- and 4-cell stages (Figures 1L–1N; Video S2). The paths of invasively migrating cells were not directionally cohesive. Leader cells intercalated often while continuously progressing the invasion front, as has been previously observed with the MDA-MB-231 cell line.[24] The non-cohesive migration of these collectively invading cells is reminiscent of prior observations of reduced next-neighbor coordination in multicellular movements when E-cadherin expression is diminished.[25] We also measured the rectilinear persistence ratio for invasive cells, which quantified the proportion of time cells migrated consistently without changing direction (<90° from previous direction). Invasive cells changed direction more often than rotational cells (Figure 1K). This established that neoplastic cells have the capacity to undergo ICM and RCM to establish ductal-like and acinus-like tissue structures in a confining ECM.

RCM and ICM do not require adherens junctions and are associated with laminin deposition

Observation of coherent angular rotations in neoplastic cells that lack any cadherin-based junctions (Figure 2A) contradicts previous reports. So, we next assessed the generality of our findings. First, we asked whether confining normal epithelial cells with proper E-cadherin junctions as well as other neoplastic epithelial cells without such cadherin junctions could produce both ductal-like and acinus-like structures. We cultured normal mammary epithelial cells, MCF-10As (Figure 2B), which have high junctional E-cadherin expression (Figure 2C), and malignant hepatocarcinoma cells, SK-HEP-1s (Figure 2D), which lack junctional cadherin expression (Figures 2E and 2F), in high-density collagen I. After 7 days in culture, we found that both cell lines were able to form the two phenotypes with varying frequencies (Figures 2G and 2H). In comparison to MDA-MB-231, which predominantly formed the ductal-like phenotype (Figure 1F), SK-HEP-1 and MCF-10A predominantly formed the acinus-like phenotype (Figures 2I and 2J). RCM and ICM behaviors were conserved in the SK-HEP-1 cells (Figures 2K–2M; Video S3), and have been previously observed in MCF-10A cells.[1,2,26–28] However, previous observations of ICM by MCF10a cells show it is directed by leader cells with E-cadherin-based cell-cell junctions,[28] which is distinct from the intercalating ICM pattern we observe in the neoplastic cells lacking cadherins junctions. Interestingly, a few of the MDA-MB-231 cells undergoing RCM matured into a hollow or toroidal acinus morphology with a distinct lumen structure (Figure 2N). Altogether, these data demonstrate that both normal and malignant epithelial cells can undergo both RCM and ICM with and without cadherin-based cell-cell adhesions. Therefore, adherens junctions are not essential for the emergence of RCM and ICM behaviors in the context of 3D confinement.

We also asked whether the assembly of an endogenous laminin-rich basement membrane was associated with either migration phenotype. Laminin-332 is an isoform highly expressed in epithelial basement membranes.[29] Immunostaining analyses of laminin-332 in the neoplastic MDA-MB-231s at 2 and 7 days after seeding revealed that both acinus-like and ductal-like structures deposit laminin over the course of a week (Figures 2O and 2P). This suggests that laminin deposition is not a unique characteristic of either migration phenotype and also indicates that neoplastic cells can deposit laminin.

A cellular Potts model predicts that RCM and ICM can arise solely from differences in local versus global matrix remodeling

Next, we sought to gain a deeper understanding of how cells of the same type in the same confining conditions can spontaneously undergo RCM or ICM. Given the multitude of cell-cell and cell-ECM interactions at play in collective migration, we first took a mathematical modeling approach. Specifically, we sought a modeling framework with which we could ask how cell polarization, cell-cell adhesion, and matrix remodeling can each contribute to the emergence of RCM and ICM in confining ECM conditions. The cellular Potts model (CPM) is a computational modeling framework that is particularly versatile in its ability to represent various biological phenomena and incorporate them to examine emergent multicellular behaviors.[30] To model cell dynamics, the CPM relies on minimization of the overall energy of the system using the Hamiltonian (H), and in its earliest application, it was used to simulate cell sorting by assuming differential adhesion between different cell types.[30,31] We built upon these previously described models by incorporating additional terms for cell motility, cell-ECM interactions, and proliferation (see STAR Methods for details) (Figure 3A). Notably, we created a cell polarization vector (P) to model the polarization of the actin cytoskeleton, where a cell's orientation and propulsion intensity are dependent on the rate of production (k^+) and the rate of degradation (k^-) of the polarization vector. The relationship between the two rates, k^+/k^-, is defined as the polarization persistence (γ), which determines how quickly the direction of the polarization vector is updated. We also defined a matrix-remodeling agent (E) that is active either locally (k_l) in the direction of the polarization vector or globally (k_g) over the whole-cell body. For k_l remodeling, each individual cell only releases the agent locally at the tip of the cell, as determined by the

Please cite this article in press as: Ranamukhaarachchi et al., Global versus local matrix remodeling drives rotational versus invasive collective migration of epithelial cells, Developmental Cell (2024), https://doi.org/10.1016/j.devcel.2024.11.021

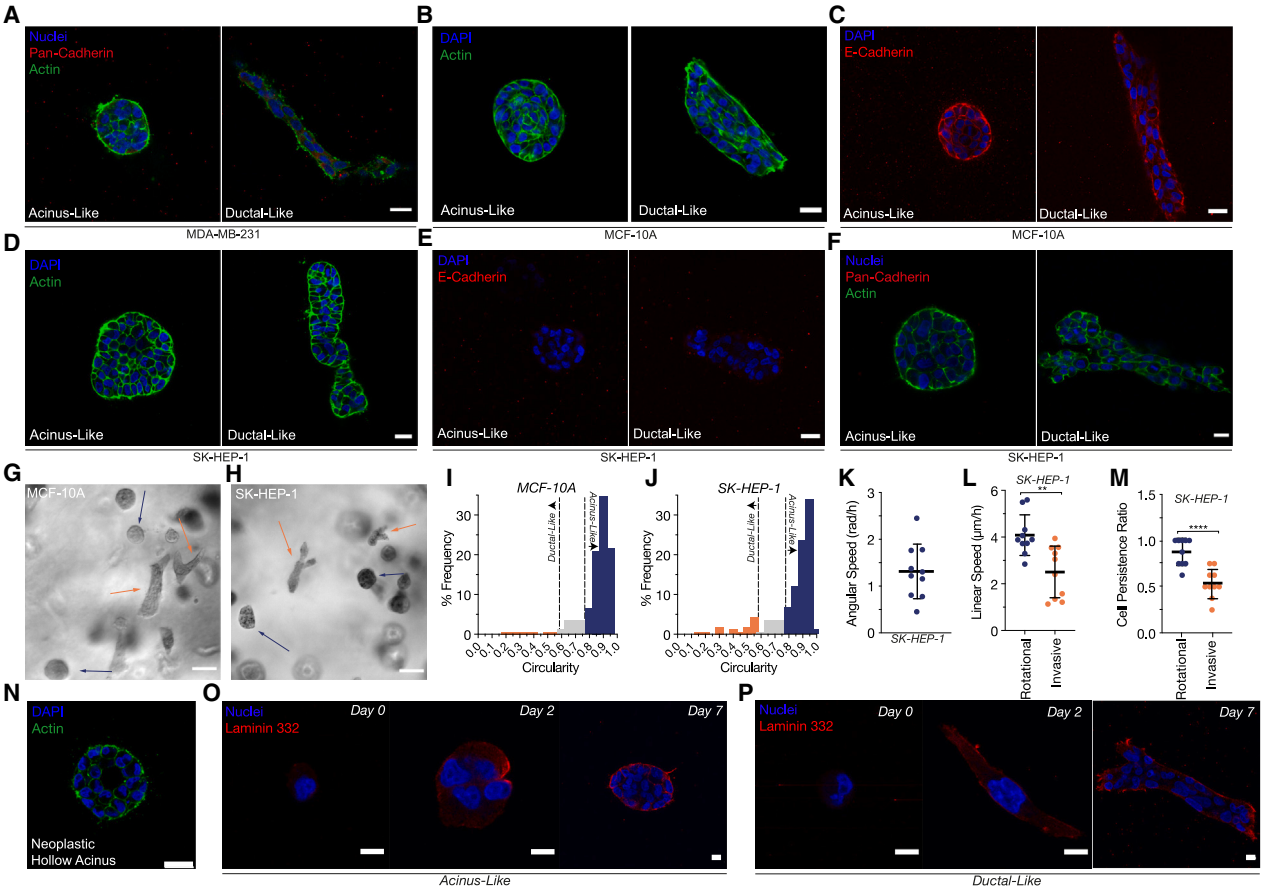

Figure 2. RCM and ICM do not require adherens junctions and are associated with laminin deposition

(A) Pan-cadherin staining of MDA-MB-231 in either acinus-like or ductal-like structures. Scale bar, 25 μm.

(B) Actin cytoskeleton staining of MCF-10A acinus-like and ductal-like structures. Scale bar, 25 μm.

(C) E-cadherin staining of MCF-10A cells in both ductal-like and acinus-like phenotypes. Scale bar, 25 μm.

(D) Actin cytoskeleton staining in SK-HEP-1 acinus-like and ductal-like structures. Scale bar, 25 μm.

(E) E-cadherin staining of SK-HEP-1 cells in both ductal-like and acinus-like phenotypes. Scale bar, 25 μm.

(F) Pan-cadherin staining of SK-HEP-1 in either acinus-like or ductal-like structures. Scale bar, 25 μm. (G and H) Bright-field images taken 7 days after seeding for (G) MCF-10A cells and (H) SK-HEP-1 cells. Orange arrows indicate ductal-like structures, and blue arrows indicate acinus-like structures. Scale bar, 100 μm. (I and J) Frequencies of ductal-like and acinus-like morphologies at 7 days in (I) MCF-10A (n = 167 multicellular structures) and (J) SK-HEP-1 (n = 165 multicellular structures) cell lines.

(K) Average angular speed per cellular track of rotational SK-HEP-1 cells in 2-cell clusters (n = 10 individual cells, n = 5 cell clusters).

(L) Average rectilinear speed per cellular track of invasive and rotational SK-HEP-1 cells in 2-cell clusters (n = 10 individual cells, n = 5 cell clusters).

(M) Cell persistence ratio per cellular track for SK-HEP-1 rotational and invasive 2-cell clusters (n = 10 individual cells per group, n = 5 cell clusters per group).

(N) A hollow acinus morphology with a distinct lumen structure formed by MDA-MB-231 cells. Scale bar, 25 μm. (O and P) Laminin-332 is deposited along the periphery of both (O) acinus-like and (P) ductal-like structures through 7 days. Scale bar, 10 μm. All error bars represent standard deviation from the mean. Statistical significance is indicated as ns, not significant, (*) $p \leq 0.05$, (**) $p \leq 0.01$, (***) $p \leq 0.001$, and (****) $p \leq 0.0001$.

direction of P, and only when the cell element is in contact with an ECM element. In remodeling with k_g, the agent release is non-directional and over the whole-cell body.

Current dogma suggests that cells require cytoskeletal polarization for ICM and RCM.[18,19] So, we first asked whether varying polarization persistence while holding all other parameters constant could give rise to both collective behaviors. For this initial simulation, cell-cell ($J_{c,c}$) and cell-ECM ($J_{c,e}$) adhesion strengths were set equal, but below the cell-medium interfacial tension ($J_{c,m}$) because setting $J_{c,m} > J_{c,c}$ and $J_{c,m} > J_{c,e}$ is important for matching the initial circular cell morphology observed in experimental settings.[15] To account for differences in matrix-remodeling agent (E) flux due to distinct spatial patterns of release, globally versus locally, we set initial values of k_g and k_l constants at a ratio of 1:10 to maintain an equivalent total concentration. Our simulations found that in conditions of high polarization persistence ($k^+ > k^-$), where the polarization vector degrades slowly, cells migrated linearly and adopted predominantly an ICM behavior (Figure 3B; Video S4A). Conversely, in conditions of lowered γ when degradation ($k^+ < k^-$) of the polarization vector dominates, cells changed direction quickly and established RCM. However, the polarization persistence and local matrix-remodeling parameters are coupled, so increasing polarization persistence also increases localized accumulation of the

Please cite this article in press as: Ranamukhaarachchi et al., Global versus local matrix remodeling drives rotational versus invasive collective migration of epithelial cells, Developmental Cell (2024), https://doi.org/10.1016/j.devcel.2024.11.021

CellPress
OPEN ACCESS

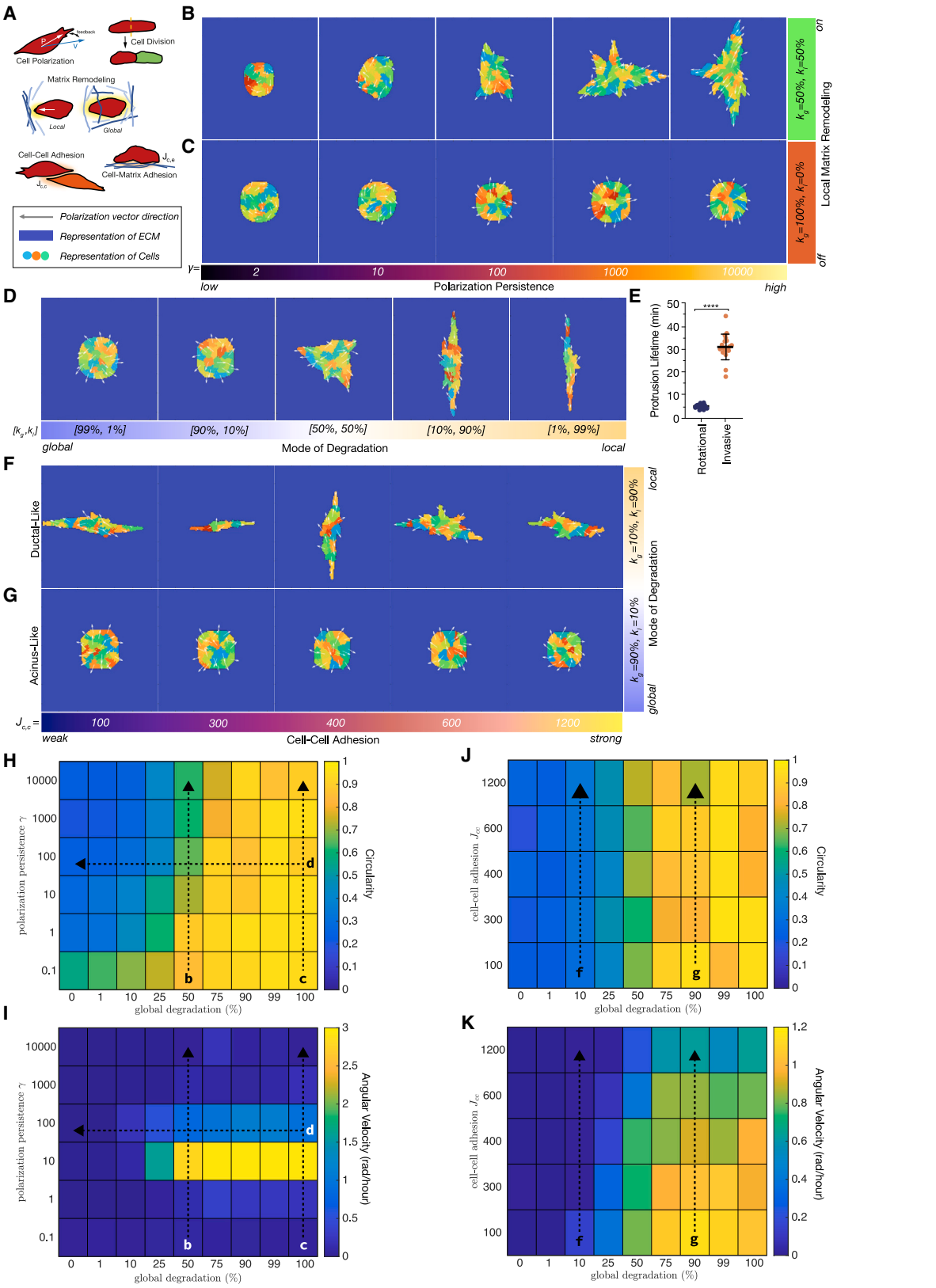

(legend on next page)

Please cite this article in press as: Ranamukhaarachchi et al., Global versus local matrix remodeling drives rotational versus invasive collective migration of epithelial cells, Developmental Cell (2024), https://doi.org/10.1016/j.devcel.2024.11.021

matrix-remodeling agent at the tip of the cell. To assess whether varying polarization persistence in the absence of local matrix degradation could still give rise to both collective behaviors, we set $k_l = 0$ and $k_g = 50$ to maintain only global production of matrix-remodeling agent (E). Conducting a parameter sweep of γ, we found that only RCM could be replicated when k_l was turned off (Figure 3C; Video S4B). In conditions of high γ, we now observed that cells failed to exhibit ICM and instead formed rounded acinus-like structures. This suggests that high polarization persistence can give rise to ICM, but only in the presence of localized matrix remodeling. Conversely, RCM arises at a relatively lower polarization persistence and does not require localized matrix remodeling.

Given these observations, we further investigated how differences in matrix remodeling play a role in directing ICM and RCM behaviors. Holding γ constant at a moderate value ($\gamma = 1{,}000$), we systematically varied matrix-remodeling parameters (k_g and k_l) and held all other parameters constant. In conditions of high k_g and low k_l, cells underwent RCM and formed acinus-like morphologies over the course of 7-day simulations (Figure 3D; Video S4C). By contrast, when local remodeling took precedence ($k_l > 50\%$), the cells degraded the matrix in the direction of the polarization vector and cellular motion, resulting in ICM behavior and ductal-like morphologies. Quantification of protrusion dynamics (see STAR Methods for details) from these simulations showed that ICM cells exhibit increased protrusion lifetime as a result of the increased local matrix remodeling (k_l), in comparison to RCM cells (Figure 3E). Together, these simulations predict that ICM and RCM rely on distinct modes of matrix remodeling and that switching from invasive to RCM requires a shift from local to global matrix remodeling. These findings also suggest that increasing the localization of matrix remodeling can increase protrusion lifetime.

Lastly, we sought to validate our experimental observation that strong cell-cell junctional strength is not essential for coordinating ICM and RCM. We selected conditions of global (k_g) and local (k_l) remodeling that induced either ICM or RCM and systematically varied the cell-cell adhesion strength ($J_{c,c}$) parameter within the conditions of each respective migration behavior. In agreement with our experimental findings, we found that varying $J_{c,c}$ while holding cell-ECM strength ($J_{c,m}$) and other parameters constant still gives rise to ICM and RCM (Figures 3F and 3G; Video S4D). The results of our 7-day CPM simulations can be summarized in phase diagrams where cell cluster circularity and angular velocities are shown using a color scale, with blue to yellow representing a range of low to high values, respectively. The angular velocity was calculated by finding the angular distance (angle, in radian) traveled by individual cells per hour with respect to the center of mass of the cluster. Figures 3H and 3I span the global degradation percentage versus polarization persistence space. Lines labeled b-d correspond to respective simulations of Figures 3B–3D. These phase diagrams show that ICM behavior requires low global degradation. Figures 3J–3K show results in global degradation versus cell-cell adhesion space, with lines f and g corresponding to Figures 3F and 3G, respectively. They show that strong cell-cell junctional strength is not essential for coordinating ICM and RCM and that ICM is only possible for low relative global degradation rates, independent of the value of the cell-cell adhesion strength (Jc,c) parameter. In summary, we found that our CPM model reliably captures the migrational shaping of acinus-like and ductal-like morphologies through RCM and ICM and predicts that distinct modes of matrix remodeling direct RCM and ICM behaviors in confinement.

Localization of matrix remodeling and polarization distinguish the initiation of RCM and ICM

To assess the relevance of our model predictions, we characterized the cell-matrix interactions underlying RCM and ICM by performing 3D time-lapse microscopy using a previously established integrated biophysical imaging platform.[13,32] In this system, MDA-MB-231 cells with stable expression of mCherry-LifeAct were generated to visualize F-actin-rich protrusions and give three readouts of cell protrusion dynamics: protrusion lifetime, maximum protrusion length, and protrusion rate. Blue fluorescent traction force beads were embedded in the collagen matrix to enable readout of three cell traction measurements: percent (%) bead movers, the maximum bead displacement, and the instantaneous bead speed. Green fluorescent dye-quenched (DQ)-collagen, an indicator of matrix remodeling, was incorporated to provide measurement of pericellular remodeling (DQ intensity) and remodeling localization (perimeter remodeling [%]). Focusing on the time frame where collective cell migration is initiated, time-lapse microscopy was conducted roughly 36 h after seeding in dense collagen, when migrating cells were in early ~2–4 cell clusters and could be distinguished

Figure 3. A cellular Potts model predicts that RCM and ICM can arise solely from differences in local versus global matrix remodeling

(A) Schematic representation of the cell-cell and cell-ECM interaction terms incorporated into the CPM. White arrows indicate the direction of the polarization vector.

(B) Simulated 7-day phenotypes of increasing polarization persistence (γ) in the presence of local (k_l) and global (k_g) matrix remodeling. White arrows indicate the direction of the polarization vector.

(C) Simulated 7-day phenotypes of increasing polarization persistence (γ) in the absence of k_l.

(D) Simulated 7-day phenotypes of increasing global (left) or local (right) matrix remodeling at constant γ.

(E) Quantification of protrusion lifetime from simulations of constant k_g and k_l values that give rise to either RCM ($k_g = 90\%$, $k_l = 10\%$) or ICM ($k_g = 10\%$, $k_l = 90\%$) behaviors ($n = 20$ multicellular structures). (F and G) Simulated 7-day phenotypes of increasing cell-cell adhesion ($J_{c,c}$), given constant k_g and k_l values that give rise to either (F) ICM or (G) RCM behaviors. Error bars represent standard deviation from the mean. (H and I) Phase diagrams summarizing (H) cell cluster circularity and (I) angular velocities as functions of global degradation percentage versus polarization persistence using a color scale, with blue to yellow representing a range of low to high values, respectively. Lines labeled b–d correspond to respective simulations of (B)–(D), with arrow directions on the phase diagram representing left to right across each respective panel. (J and K) Phase diagrams summarizing (J) cell cluster circularity and (K) angular velocities as functions of global degradation versus cell-cell adhesion space using a color scale, with blue to yellow representing a range of low to high values, respectively. Lines f and g correspond to (F) and (G), respectively, with arrow directions on the phase diagram representing left to right across each respective panel. Statistical significance is indicated as ns, not significant, (*) $p \leq 0.05$, (**) $p \leq 0.01$, (***) $p \leq 0.001$, and (****) $p \leq 0.0001$.

Please cite this article in press as: Ranamukhaarachchi et al., Global versus local matrix remodeling drives rotational versus invasive collective migration of epithelial cells, Developmental Cell (2024), https://doi.org/10.1016/j.devcel.2024.11.021

CellPress
OPEN ACCESS

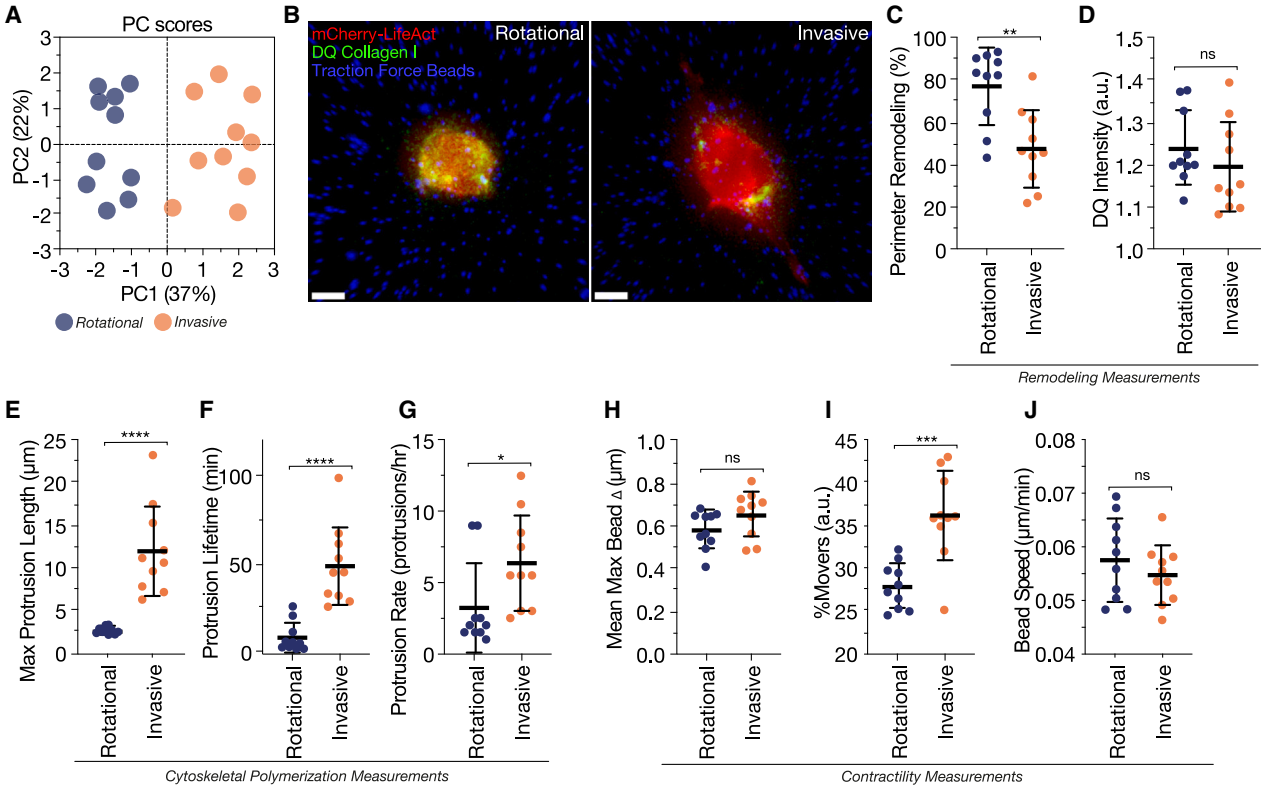

Figure 4. Localization of matrix remodeling and polarization distinguishes the initiation of RCM and ICM

(A) PCA plot of biophysical metrics. Blue data points represent rotational cells and orange represent invasive cells.

(B) Micrographs of MDA-MB-231 cells with stable expression of mCherry-LifeAct, blue fluorescent traction force beads, and green fluorescence of DQ-collagen I incorporated in the surrounding collagen matrix. Scale bar, 10 μm. (C and D) Quantification of (C) % pericellular matrix remodeling and (D) pericellular matrix-remodeling intensity, as measured by DQ-collagen I. (E–G) Quantification of (E) maximum protrusion length, (F) average protrusion lifetime, and (G) protrusion formation rate, as measured by mCherry-LifeAct. (H–J) Quantification of (H) average maximum bead displacement, (I) average % moving beads, and (J) bead speed, as measured by traction force beads. For all plots, $n = 10$ rotationally migrating cell clusters and $n = 10$ invasively migrating cell clusters. All error bars represent standard deviation from the mean.

Statistical significance is indicated as ns, not significant, (*) $p \leq 0.05$, (**) $p \leq 0.01$, (***) $p \leq 0.001$, and (****) $p \leq 0.0001$.

by circularity (Figure 1F). Mapping these eight biophysical measurements into 2D space using principal-component analysis (PCA) separated and clustered the two phenotypes, indicating that our multiplexed biophysical analysis platform captured underlying differences in cell-ECM interactions between RCM and ICM (Figure 4A).

A closer look revealed that DQ-collagen signal was localized primarily to the base of protrusions in ~60% of invasive cells, while rotationally migrating cells exhibited a global pattern of DQ signal with significantly higher perimeter remodeling (Figures 4B, 4C, S1A, and S1B). Interestingly, there was no appreciable difference in the pericellular DQ intensity, as measured by the average background-normalized DQ fluorescence intensity within a 5 μm band along the periphery of the cell structures (Figure 4D). These findings are consistent with model predictions that show that differences in matrix-remodeling localization produce divergent modes of collective cell migration (Figure 3D). Comparison of protrusion dynamics showed that invasively migrating cells produced longer, longer-lived protrusions at a higher rate than rotationally migrating cells, which were instead characterized by short, shorter-lived protrusions produced at a lower rate (Figures 4E–4G; Videos S5 and S6; Figures S1A and S1B). This matched quantifications of protrusion lifetime from simulated ICM and RCM cells with high or low localization of matrix remodeling, respectively (Figure 3E). While bead tracking revealed no appreciable differences in terms of maximum bead displacement and bead speed, the invasive phenotype was characterized by having higher % bead movers (Figures 4H–4J). This suggests that the invasive phenotype may have greater traction than the rotational phenotype. Overall, this experimental evidence agrees with model predictions that implicate matrix-remodeling localization, protrusion length, and protrusion lifetime as key factors that are differentially coordinated to achieve ICM versus RCM behaviors. More specifically, our cells may occupy CPM-simulated states along line d in Figures 3H and 3I, based on circularity, angular velocity, and protrusion lifetime measurements. The invasive phenotype is propagated by elongated cells with longer-lived protrusions and localized matrix remodeling, while the rotational phenotype is propagated by rounded cells with shorter-lived protrusions and global matrix remodeling.

Please cite this article in press as: Ranamukhaarachchi et al., Global versus local matrix remodeling drives rotational versus invasive collective migration of epithelial cells, Developmental Cell (2024), https://doi.org/10.1016/j.devcel.2024.11.021

ICM but not RCM-associated matrix remodeling is dependent on MMPs

Having established that the formation of acinus-like and ductal-like morphologies originates from distinct patterns of matrix remodeling, we next explored the underlying mechanistic differences regulating these modes. Matrix remodeling is known to occur through both proteolytic and physical mechanisms, and prior work has suggested that DQ-collagen I may be a readout of both.[5,21,22,33] Migration tracking at the 2-cell stage revealed that MMP inhibitor (MMPi)-treated cells maintained a rounded shape and migrated rotationally with no appreciable differences in angular speed and persistence to the control rotational cells (Figures 5A–5G; Video S7).

As a functional readout of MMP inhibition, we compared the DQ intensity and perimeter localization patterns between control invasive, control rotational, and MMPi rotational cells. Surprisingly, MMPi-treated cells generated pericellular DQ signals of greater intensity than invasive control cells (Figure 5H) with a matrix remodeling pattern similar to control rotational cells (Figure 5I). Further investigation using an antibody specific to MMP-cleaved collagen I (Col $^{3}/_{4}$) showed that control invasive cells exhibited higher MMP-dependent remodeling than control rotational cells. As expected, MMPi-treated rotational cells exhibited significantly less MMP-dependent remodeling (Figures 5J and 5K). These data indicate that ICM, but not RCM, is dependent on local MMP-dependent proteolytic matrix remodeling. It is important to note that DQ-collagen I is not as sensitive as the Col $^{3}/_{4}$ antibody for detecting MMP-cleaved collagen I (Figure S2).

MT1-MMP is a membrane-tethered MMP that is trafficked to protrusions at the cell's advancing front in order to drive invasion in normal and neoplastic cells.[21,34–36] We next asked whether MT1-MMP may be localized differently between the RCM and ICM cells given their differences in matrix-remodeling localization and MMP-dependent remodeling (Figure 4C). Immunostaining analysis revealed an increase in localization of MT1-MMP to the ends of protrusion in ICM cells, whereas RCM cells exhibited a global pattern of MT1-MMP along the pericellular membrane, as measured by signal distribution skewness (Figures 5L and 5M). Interestingly, the localization of MT1-MMP to the ends of protrusions in ICM cells is distinct from their DQ-collagen I signal, which localized primarily to the base of protrusions (Figures 4B and 4C). Trafficking of MT1-MMP to sites of invasive protrusions is known to be mediated by integrin beta 1 (ITGβ1) localization.[21,37] As such, we next asked whether ITGβ1 localization in ICM and RCM cells mimics the distribution of MT1-MMP. Immunostaining analysis of ICM cells revealed slightly more focalized ITGβ1 near protrusion tips, whereas RCM cells showed more of a global distribution of ITGβ1 (Figures 5L and 5N).

We next asked whether inhibition of MMP activity may alter MT1-MMP and ITGβ1 localization since MMPi treatment enriched for RCM. Signal distribution analysis of MT1-MMP and ITGβ1 immunostaining revealed that MMPi-treated cells were unable to focalize MT1-MMP or ITGβ1 and instead exhibited a global staining pattern for both proteins similar to vehicle-treated rotational cells (Figures 5L–5N). Local ITGβ1 and MT1-MMP activity is known to facilitate the formation of invasive protrusions,[21,37] so we next characterized actin-based protrusion dynamics in these cells. MMPi-treated rotational cells exhibited significantly lower protrusion length, lifetime, and rate compared with control ICM cells but were similar to control RCM cells (Figures 5O–5Q). This leads us to speculate that in confining conditions, localized MMP-mediated matrix-remodeling activity promotes increased protrusion length, lifetime, and actin polarization, which exerts positive feedback on MT1-MMP and ITGβ1 trafficking and focalization. However, MMPs have recently been shown to mediate cleavage of numerous intracellular protein targets involved in cytoskeletal regulation, including alpha-actinin, talin, and pericentrin.[38–41] As such, treatment of cells with MMPi could have direct effects on the cytoskeleton. To investigate whether the reduced protrusion dynamics and global matrix-remodeling pattern observed in MMPi-treated cells could be driven by direct effects on cytoskeletal protein abundance, we conducted western blot analysis of the known intracellular protein targets of MMPs. No significant changes in abundance were observed in MMPi-treated cells relative to the vehicle control condition (Figure S3). Thus, these data demonstrate that ICM, but not RCM, is dependent on local MMP-dependent proteolytic matrix remodeling and that proteolytic remodeling activity feeds back on actin cytoskeleton activities as well as MT1-MMP and ITGβ1 trafficking.

RCM relies on ITGβ1

Given that MMPi-treated cells underwent RCM and maintained the ability to significantly remodel the matrix in an isotropic manner, we hypothesized that RCM may rely on physical mechanisms of remodeling. Tracking of bead displacements showed that control and MMPi RCM cells maintained comparable traction (Figures 5R–5T). This suggested that RCM MMPi cells were physically contracting the matrix (Video S8; Figure S1C) and led us to hypothesize that global remodeling during RCM may be mediated by adhesion-based traction forces on the matrix. ITGβ1 is the canonical cell adhesion receptor for collagen I. To assess the relevance of ITGβ1 to remodeling by rotational cells, we performed ITGβ1 deletion using CRISPR-Cas9 in the MDA-MB-231 cell line (crITGβ1; Figure 6A). Similar to previous ITGβ1-blocking studies, we found that crITGβ1 promoted a rounded phenotype and enrichment of acinus-like structures 7 days after seeding (Figure 6B).[42] To identify whether adhesion was necessary for RCM, we tracked crITGβ1 cells every hour for 10 h at the 2-cell stage and found that rotational migration was abrogated, as cells failed to undergo coherent rotations (Figure 6C; Video S9). To determine whether adhesion contributes to pericellular matrix remodeling, we analyzed pericellular DQ intensity 48 h after seeding. This showed that crITGβ1 cells had significantly diminished pericellular matrix remodeling compared with wild-type (WT) vehicle and WT MMPi cells (Figures 6D and 6E). Inhibiting MMPs in crITGβ1 did not further diminish matrix-remodeling signal. Given that DQ-collagen I signal does not fully capture MMP-cleaved collagen signal, and ITGβ1 is a known regulator of MT1-MMP,[37] we next assessed whether crITGβ1 may have indirectly affected matrix remodeling through regulation of MT1-MMP expression.[43] Western blot analysis of MT1-MMP in crITGβ1 cells showed no appreciable changes in abundance relative to the WT control (Figure 6F). Analysis of MMP-cleaved matrix

Please cite this article in press as: Ranamukhaarachchi et al., Global versus local matrix remodeling drives rotational versus invasive collective migration of epithelial cells, Developmental Cell (2024), https://doi.org/10.1016/j.devcel.2024.11.021

CellPress
OPEN ACCESS

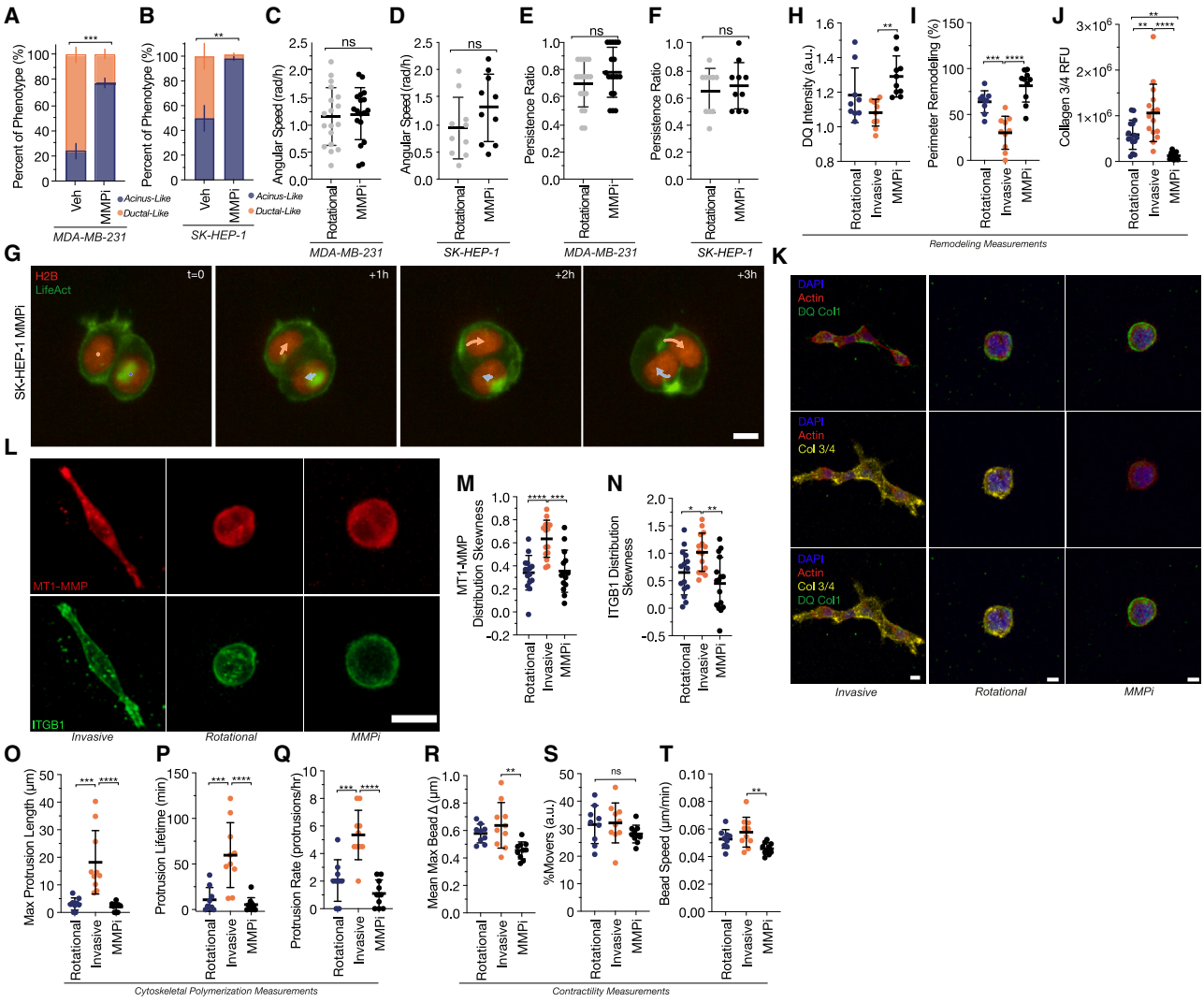

Figure 5. ICM but not RCM is dependent on MMP-mediated matrix remodeling

(A and B) Frequencies of ductal-like and acinus-like morphologies at 7 days in vehicle- and MMPi-treated (A) MDA-MB-231 (n = 217 multicellular structures and n = 192 multicellular structures for vehicle and MMP-treated conditions, respectively) and (B) SK-HEP-1 cell lines (n = 207 multicellular structures and n = 220 multicellular structures for vehicle and MMP-treated conditions, respectively). (C and D) Average angular speed per cellular track of vehicle- and MMPi-treated (C) MDA-MB-231 (n = 18 individual cells, n = 9 cell clusters per treatment condition) and (D) SK-HEP-1 cells in 2-cell clusters (n = 8 individual cells, n = 4 cell clusters per treatment condition). (E and F) Cell persistence ratio per cellular track for vehicle- and MMPi-treated (E) MDA-MB-231 (n = 18 individual cells, n = 9 cell clusters per treatment condition) and (F) SK-HEP-1 cells in 2- cell clusters (n = 8 individual cells, n = 4 cell clusters per treatment condition).

(G) Time-lapse images of circular 2-cell clusters of SK-HEP-1 MMPi-treated cells reveals persistent rotational migration. Scale bar, 10 μm. (H and I) Quantification of (H) pericellular matrix-remodeling intensity and (I) % pericellular matrix remodeling, as measured by DQ-collagen I.

(J) Quantification of MMP-dependent remodeling, using the collagen $^{3}/_{4}$ antibody specific to MMP-cleaved collagen I (n = 15 cells per condition were analyzed from three independent biological replicates).

(K) Representative fluorescent micrographs show matrix remodeling of vehicle-treated invasive and rotational and MMPi-treated rotational MDA-MB-231 cells, as measured by DQ-collagen I and collagen $^{3}/_{4}$ antibody. Scale bar, 10 μm.

(L) Representative fluorescent micrographs show MT1-MMP and ITGβ1 signal distribution in vehicle-treated invasive and rotational and MMPi-treated rotational MDA-MB-231 cells. Scale bar, 25 μm. (M and N) Quantification of (M) MT1-MMP and (N) ITGβ1 signal distribution along pericellular membranes of vehicle-treated invasive and rotational and MMPi-treated rotational MDA-MB-231 cells, as quantified by MT1-MMP signal distribution skewness (n = 14–15 cells per condition were analyzed from three independent biological replicates). (O–Q) Quantification of (O) maximum protrusion length, (P) average protrusion lifetime, and (Q) protrusion formation rate, as measured by mCherry-LifeAct. (R–T) Quantification of (R) average maximum bead displacement, (S) average % moving beads, and (T) bead speed, as measured by traction force beads. For graphs (H, I, and O–T) n = 9–10 cells were analyzed per condition. All error bars represent standard deviation from the mean.

Statistical significance is indicated as ns, not significant, (*) $p \leq 0.05$, (**) $p \leq 0.01$, (***) $p \leq 0.001$, and (****) $p \leq 0.0001$.

Please cite this article in press as: Ranamukhaarachchi et al., Global versus local matrix remodeling drives rotational versus invasive collective migration of epithelial cells, Developmental Cell (2024), https://doi.org/10.1016/j.devcel.2024.11.021

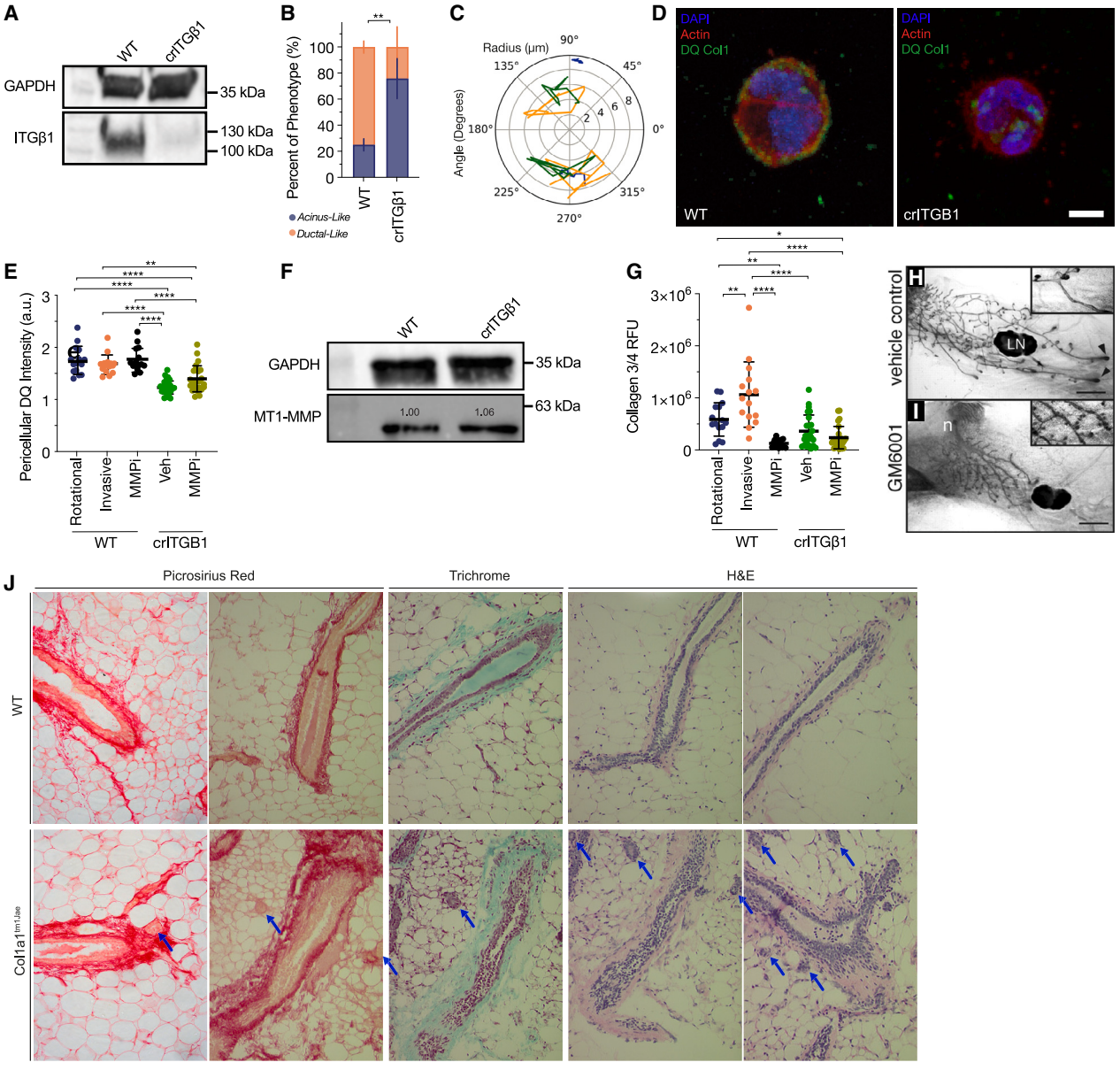

Figure 6. RCM relies on ITGβ1

(A) Western blot assessment of *ITGβ1* depletion in MDA-MB-231 cell line.

(B) Frequencies of ductal-like and acinus-like morphologies at 7 days in WT and crITGβ1 MDA-MB-231 cells (n = 139 multicellular structures and n = 141 multicellular structures for WT and crITGβ1 cell lines, respectively).

(C) Polar plots of rounded 2-cell clusters of MDA-MB-231 crITGβ1 cells (n = 6 individual cells, n = 3 cell clusters), and color indicates cluster pair.

(D) Representative fluorescent micrographs show matrix-remodeling localization at 48 h of rounded WT and crITGβ1 MDA-MB-231 cells, as measured by DQ-collagen I. Scale bar, 10 μm.

(E) Quantification of pericellular matrix-remodeling intensity, as measured by DQ-collagen I (n = 15 cells for all WT conditions, n = 25 for all crITGβ1 conditions).

(F) Western blot assessment MT1-MMP expression in MDA-MB-231 WT and crITGβ1 cells. Values on blot indicate quantified relative MT1-MMP expression.

(G) Quantification of MMP-dependent remodeling, using the collagen $^{3}/_{4}$ antibody specific to MMP-cleaved collagen I. n = 15 cells for all WT conditions, n = 25 for all crITGβ1 conditions. All error bars represent standard deviation from the mean. (H and I) Histology of whole-mount mammary glands from 6.5-week-old mice treated daily with (H) vehicle or (I) GM-6001 broad-spectrum MMP inhibitor from 3.5 weeks old reveals increased lateral budding in GM6001-treated mammary glands. Scale bar, 1 mm. Image reproduced with permission: ©2003 Wiseman et al.[44] Originally published in *Journal of Cell Biology*. https://doi.org/10.1083/jcb.200302090 as Figures 2a and 2b.

(J) Histology of mammary tissue from wild-type control (left column) and Col1a1tm1Jae (right column) mice showing increased prevalence of spheroid structures (arrows) in Col1a1tm1Jae mammary tissue. Collagen surrounding the mammary duct is detected with H&E, trichrome, and picrosirius red staining. Images taken from Provenzano et al.[46] Figures 3a and 3c and Supplementary Figures 2a and 2b, which was published in *BMC Medicine* in 2006 with a Creative Commons CC BY license (https://doi.org/10.1186/1741-7015-4-38).

Statistical significance is indicated as ns, not significant, (*) $p \leq 0.05$, (**) $p \leq 0.01$, (***) $p \leq 0.001$, and (****) $p \leq 0.0001$.

Please cite this article in press as: Ranamukhaarachchi et al., Global versus local matrix remodeling drives rotational versus invasive collective migration of epithelial cells, Developmental Cell (2024), https://doi.org/10.1016/j.devcel.2024.11.021

CellPress
OPEN ACCESS

remodeling also confirmed that crITGβ1 cells could generate similar levels of MMP-cleaved collagen to WT cells (Figure 6G). Altogether, this suggests that rotational migration is dependent on ITGβ1-based adhesion to the matrix, and this adhesion may give rise to physical remodeling as a result of rotational movements. However, we cannot exclude the possibility that ITGβ1 plays a role in mediating the secretion of non-MMP enzymes that could potentially participate in matrix remodeling.

Acinus-like structures develop in virgin mouse mammary tissue upon inhibition of MMP-mediated ECM remodeling

To test the *in vivo* relevance of our findings, we analyzed tissue histology from previously published studies wherein the mammary glands of virgin mice were treated with the broad-spectrum MMP inhibitor GM6001 (Figures 6H and 6I). In MMP-inhibitor-treated tissues, mammary ducts showed less invasion than controls, but also spherical acinus-like structures appeared alongside the primary ducts (Figure 6I).[44] This tissue architecture was distinct from mammary tissues of control virgin mice, which displayed a normally sparse and isolated ductal epithelium within large areas of mammary fat pad (Figure 6H).

Since MMPs can have additional functions other than matrix remodeling, we also asked whether an *in vivo* model of reduced collagen degradation would yield similar results. The Col1a1^{tm1Jae} mouse produces collagen type I that is resistant to degradation by MMPs due to a mutation in a collagen cleavage site.[45] Degradation-resistant collagen should functionally mimic the effect of inhibiting MMP activity on matrix remodeling more specifically. In histological sections of Col1a1^{tm1Jae} mammary tissues, we observed an altered mammary architecture that is similar to MMP-inhibited mammary glands: spherical lobular-like structures appeared near ducts (Figure 6J).[46] These findings are also synergistic with our previous work, which showed that the formation of spherical acinus-like structures emerged spontaneously in low-density Col1 hydrogels that were made less degradable by macromolecular crowding-induced changes to fibril architecture.[14] These data provide evidence connecting our *in vitro* findings and model system to *in vivo* behaviors and settings.

DISCUSSION

Our study suggests that early differences in the localization and mechanism of matrix remodeling dictate cell shape and cytoskeletal polarization, which are inherited across cell divisions to give rise to different collective migration behaviors. Localized remodeling driven by enzymatic cleavage dependent on MMPs gives rise to long protrusions that are long-lived and results in ICM. Global remodeling mediated by ITGβ1 limits protrusion length and lifetime and results in RCM. Inhibition of MMP-mediated matrix cleavage does not abrogate collective migration but instead biases cells toward global remodeling and RCM while promoting global localization of ITGβ1 and MT1-MMP. It is interesting to consider the effect of adhesion distribution on overall adhesion strength. Our observations of differences in spatial distribution of ITGβ1 suggest that RCM cells may be more isotropically adhesive, whereas ICM cells may be more anisotropically adhesive. Additionally, the adherence of ICM cells to the matrix at fewer sites may contribute to ITGβ1 and MT1-MMP being enriched at those locations to promote local MMP-dependent proteolytic remodeling. If fewer sites of adhesion translate to less overall adhesion strength, then our findings would be consistent with previous work showing that less adhesive cells are more invasive[47] and that reducing adhesion with an ITGβ1 blocking antibody can promote more persistent invasive migration and an association between protrusion length and DQ matrix degradation.[32] However, since blocking MMP activity globalizes matrix remodeling, MT1-MMP, and ITGβ1, the initial creation of space in the matrix for a protrusion to extend into may be the initial step that provides feedback on both integrin and MT1-MMP activity. This feedback may determine the dominance of global physical or local proteolytic remodeling activity in driving RCM versus ICM behaviors. Additional studies to temporally apply key perturbations, such as MMP inhibition and ITGβ1 blocking, may lend further insight into the initiating steps of these distinct collective behaviors.

Our analysis shows that RCM and ICM collective migration behaviors are conserved across both normal and neoplastic epithelial cells with and without cadherin-based cell-cell junctions when embedded within a confining ECM. This shifts the current paradigm, which holds that the initiation of RCM behaviors requires adherens junctions. Our findings suggest that many of the mechanisms governing normal epithelial collective migration may be hijacked by neoplastic epithelial cells when presented with appropriate matrix cues. Coherent rotational migration of normal mammary acini has been linked to the establishment of apical-basal polarity through the assembly of an endogenous laminin-rich basement membrane.[2] Likewise, ICM of normal myoepithelial cells during branching morphogenesis of the mammary gland involves degradation of the existing ECM and the secretion of new basement membrane components to form a secondary ECM around new branches.[48] We found laminin-332 deposition in development of both acinus-like and ductal-like structure, suggesting that basement membrane assembly is not a unique characteristic of either migration phenotype and indicating that neoplastic cells can deposit laminin. This finding contradicts a previous report that attributes the inability of neoplastic cells to undergo RCM to their failure to deposit a laminin-rich basement membrane.[2] Additionally, the ability of collectively invasive cells to deposit basement membrane proteins seemingly defies the fundamental definition of cancer invasion as a breach of the basement membrane. However, this may reflect the ability of some invasive carcinomas to display a continuous basement membrane *in vivo*.[49]

Interestingly, previous studies have also indicated that neoplastic epithelial cells are unable to establish lumen-like hollowness, unlike normal MCF10a cells.[1,2,50,51] Our observations of MDA-MB-231 cells maturing into a hollow acinus morphology suggest that cancer cells can mimic normal acinus formation through confinement-induced RCM, which may relate to rare acinar cell carcinomas.[10,11]

Our CPM provided a powerful computational framework to explore how each cell-cell and cell-ECM interaction contributed to the emergence of RCM and ICM in confining ECM conditions. Additional states predicted by simulations may be experimentally

Please cite this article in press as: Ranamukhaarachchi et al., Global versus local matrix remodeling drives rotational versus invasive collective migration of epithelial cells, Developmental Cell (2024), https://doi.org/10.1016/j.devcel.2024.11.021

valid with adequate exploration and tuning of the parameter space. The CPM may also be a useful tool for applications in tissue engineering, such as controlled organoid patterning, by providing a framework to predict and guide collective cell behaviors through careful tuning of matrix and cell parameters.

Our findings highlight that the mechanisms governing collective cell migration are context dependent, and heterogeneity of collective migration phenotypes can be driven by divergent matrix-remodeling strategies that emerge in response to physical confinement.

Limitations of the study

Our study identifies two distinct matrix-remodeling modes adopted by epithelial cells in confining 3D environments that drive RCM and ICM. Matrix remodeling is a context-dependent behavior that is expected to be influenced by the extent of 3D ECM confinement as well as cell and matrix type. It will be important to further investigate these factors and to better define confinement with both ECM and cellular contributions. Since MMP inhibition promoted global localization of MT1-MMP and ITGβ1 and resulted in RCM, it will also be important to understand how MMP activity feeds back on the trafficking of these membrane proteins. Additionally, our study did not address how ECM confinement and remodeling factors into the ability of acinar and ductal-like structures to form lumens that produce and conduct fluid, respectively. As this is necessary for tissue function, it will be an important question to follow up on in future studies.

Our analysis of tissue histology from previously published studies reveals an increase in the presence of acinus-like structures *in vivo* with inhibition of MMP-dependent ECM remodeling. Further studies are needed to confirm whether these structures are formed by RCM behaviors. It will also be important to investigate the contribution of RCM and global matrix remodeling to the pathology of acinar cell carcinomas. This may illuminate novel methods to specifically target this rare subtype found in exocrine gland cancers.

RESOURCE AVAILABILITY

Lead contact

Further information and requests for resources and reagents should be directed to and will be fulfilled by the lead contact, Stephanie Fraley (sifraley@ucsd.edu).

Materials availability

This study did not generate new unique reagents.

Data and code availability

- Microscopy data reported in this paper will be shared by the lead contact upon request.
- All original code has been deposited at Zenodo and is publicly available as of the date of publication. DOIs are listed in the key resources table.
- Any additional information required to reanalyze the data reported in this paper is available from the lead contact upon request.

ACKNOWLEDGMENTS

Support for this study was provided by National Science Foundation CAREER award MCB-1651855 to S.I.F., National Science Foundation grant DMS-1953469 to W.-J.R. and S.I.F., American Cancer Society Research Scholar grant RSG-21-033-01-CSM to S.I.F., and National Cancer Institute U54CA274502 to S.I.F. S.K.R. was supported by a National Cancer Institute postdoctoral training grant 5T32CA121938. We would like to thank the UC San Diego School of Medicine Microscopy Core, which is supported by the National Institute of Neurological Disorders and Stroke grant P30NS047101. We would like to acknowledge Badri Narasimhan for his assistance in experimental design and interpretation of findings.

AUTHOR CONTRIBUTIONS

S.K.R., A.W., W.D.L., M.-H.T., W.-J.R., and S.I.F. designed the experiments. S.K.R. and A.W. performed all wet lab experiments and analysis. S.L. performed 7-day structure analysis. M.-H.T. and W.-J.R. designed numerical simulations, and M.-H.T. performed all computational experiments and analysis. S.K.R., A.W., W.D.L., M.-H.T., W.-J.R., and S.I.F. contributed to data interpretation as well as writing and editing of the manuscript.

DECLARATION OF INTERESTS

The authors declare no competing interests.

STAR★METHODS

Detailed methods are provided in the online version of this paper and include the following:

- KEY RESOURCES TABLE
- EXPERIMENTAL MODEL AND SUBJECT DETAILS
  - Cell culture and cell transfection
- METHOD DETAILS
  - Treatment with pharmacological inhibitors
  - CRISPR-Cas9 mediated gene suppression of ITGβ1
  - 3D culture in high density collagen I matrices
  - 7 day phenotype structure quantification
  - Immunofluorescence staining
  - Imaging for migrational tracking
  - Confocal microscopy
  - Cellular Potts model simulations
  - MMP-cleaved Collagen Quantification
  - Immunostaining Distribution Quantification
  - Western blot analysis
- QUANTIFICATION AND STATISTICAL ANALYSIS

SUPPLEMENTAL INFORMATION

Supplemental information can be found online at https://doi.org/10.1016/j.devcel.2024.11.021.

Received: November 8, 2023
Revised: July 18, 2024
Accepted: November 29, 2024
Published: December 19, 2024

REFERENCES

1. Tanner, K., Mori, H., Mroue, R., Bruni-Cardoso, A., and Bissell, M.J. (2012). Coherent angular motion in the establishment of multicellular architecture of glandular tissues. Proc. Natl. Acad. Sci. USA *109*, 1973–1978. https://doi.org/10.1073/pnas.1119578109.
2. Wang, H., Lacoche, S., Huang, L., Xue, B., and Muthuswamy, S.K. (2013). Rotational motion during three-dimensional morphogenesis of mammary epithelial acini relates to laminin matrix assembly. Proc. Natl. Acad. Sci. USA *110*, 163–168. https://doi.org/10.1073/pnas.1201141110.
3. Ewald, A.J., Brenot, A., Duong, M., Chan, B.S., and Werb, Z. (2008). Collective epithelial migration and cell rearrangements drive mammary branching morphogenesis. Dev. Cell *14*, 570–581. https://doi.org/10.1016/j.devcel.2008.03.003.

Please cite this article in press as: Ranamukhaarachchi et al., Global versus local matrix remodeling drives rotational versus invasive collective migration of epithelial cells, Developmental Cell (2024), https://doi.org/10.1016/j.devcel.2024.11.021

4. Inman, J.L., Robertson, C., Mott, J.D., and Bissell, M.J. (2015). Mammary gland development: cell fate specification, stem cells and the microenvironment. Development *142*, 1028–1042. https://doi.org/10.1242/dev.087643.

5. Fernández, P.A., Buchmann, B., Goychuk, A., Engelbrecht, L.K., Raich, M.K., Scheel, C.H., Frey, E., and Bausch, A.R. (2021). Surface-tension-induced budding drives alveologenesis in human mammary gland organoids. Nat. Phys. *17*, 1130–1136. https://doi.org/10.1038/s41567-021-01336-7.

6. Haigo, S.L., and Bilder, D. (2011). Global tissue revolutions in a morphogenetic movement controlling elongation. Science *331*, 1071–1074. https://doi.org/10.1126/science.1199424.

7. Cetera, M., Ramirez-San Juan, G.R., Oakes, P.W., Lewellyn, L., Fairchild, M.J., Tanentzapf, G., Gardel, M.L., and Horne-Badovinac, S. (2014). Epithelial rotation promotes the global alignment of contractile actin bundles during Drosophila egg chamber elongation. Nat. Commun. *5*, 5511. https://doi.org/10.1038/ncomms6511.

8. Popkova, A., Stone, O.J., Chen, L., Qin, X., Liu, C., Liu, J., Belguise, K., Montell, D.J., Hahn, K.M., Rauzi, M., et al. (2020). A Cdc42-mediated supracellular network drives polarized forces and Drosophila egg chamber extension. Nat. Commun. *11*, 1921. https://doi.org/10.1038/s41467-020-15593-2.

9. Bischoff, M.C., and Bogdan, S. (2021). Collective cell migration driven by filopodia-New insights from the social behavior of myotubes. BioEssays *43*, e2100124. https://doi.org/10.1002/bies.202100124.

10. Piscuoglio, S., Hodi, Z., Katabi, N., Guerini-Rocco, E., Macedo, G.S., Ng, C.K.Y., Edelweiss, M., De Mattos-Arruda, L., Wen, H.Y., Rakha, E.A., et al. (2015). Are acinic cell carcinomas of the breast and salivary glands distinct diseases? Histopathology *67*, 529–537. https://doi.org/10.1111/his.12673.

11. Conlon, N., Sadri, N., Corben, A.D., and Tan, L.K. (2016). Acinic cell carcinoma of breast: morphologic and immunohistochemical review of a rare breast cancer subtype. Hum. Pathol. *51*, 16–24. https://doi.org/10.1016/j.humpath.2015.12.014.

12. Calimano-Ramirez, L.F., Daoud, T., Gopireddy, D.R., Morani, A.C., Waters, R., Gumus, K., Klekers, A.R., Bhosale, P.R., and Virarkar, M.K. (2022). Pancreatic acinar cell carcinoma: A comprehensive review. World J. Gastroenterol. *28*, 5827–5844. https://doi.org/10.3748/wjg.v28.i40.5827.

13. Velez, D.O., Ranamukhaarachchi, S.K., Kumar, A., Modi, R.N., Lim, E.W., Engler, A.J., Metallo, C.M., and Fraley, S.I. (2019). 3D collagen architecture regulates cell adhesion through degradability, thereby controlling metabolic and oxidative stress. Integr. Biol. (Camb) *11*, 221–234. https://doi.org/10.1093/intbio/zyz019.

14. Ranamukhaarachchi, S.K., Modi, R.N., Han, A., Velez, D.O., Kumar, A., Engler, A.J., and Fraley, S.I. (2019). Macromolecular crowding tunes 3D collagen architecture and cell morphogenesis. Biomater. Sci. *7*, 618–633. https://doi.org/10.1039/c8bm01188e.

15. Velez, D.O., Tsui, B., Goshia, T., Chute, C.L., Han, A., Carter, H., and Fraley, S.I. (2017). 3D collagen architecture induces a conserved migratory and transcriptional response linked to vasculogenic mimicry. Nat. Commun. *8*, 1651. https://doi.org/10.1038/s41467-017-01556-7.

16. Chen, K., Ozturk, K., Contreras, R.L., Simon, J., McCann, S., Chen, W.J., Carter, H., and Fraley, S.I. (2021). Phenotypically supervised single-cell sequencing parses within-cell-type heterogeneity. iScience *24*, 101991. https://doi.org/10.1016/j.isci.2020.101991.

17. Leineweber, W.D., Rowell, M.Z., Ranamukhaarachchi, S.K., Walker, A., Li, Y., Villazon, J., Mestre-Farrera, A., Hu, Z., Yang, J., Shi, L., et al. (2024). Divergent iron-regulatory states contribute to heterogeneity in breast cancer aggressiveness. iScience *27*, 110661. https://doi.org/10.1016/j.isci.2024.110661.

18. Jain, S., Cachoux, V.M.L., Narayana, G.H.N.S., de Beco, S., D'Alessandro, J., Cellerin, V., Chen, T., Heuzé, M.L., Marcq, P., Mège, R.-M., et al. (2020). The role of single cell mechanical behavior and polarity in driving collective cell migration. Nat. Phys. *16*, 802–809. https://doi.org/10.1038/s41567-020-0875-z.

19. Glentis, A., Blanch-Mercader, C., Balasubramaniam, L., Saw, T.B., d'Alessandro, J., Janel, S., Douanier, A., Delaval, B., Lafont, F., Lim, C.T., et al. (2022). The emergence of spontaneous coordinated epithelial rotation on cylindrical curved surfaces. Sci. Adv. *8*, eabn5406. https://doi.org/10.1126/sciadv.abn5406.

20. Friedl, P., Locker, J., Sahai, E., and Segall, J.E. (2012). Classifying collective cancer cell invasion. Nat. Cell Biol. *14*, 777–783. https://doi.org/10.1038/ncb2548.

21. Wolf, K., Wu, Y.I., Liu, Y., Geiger, J., Tam, E., Overall, C., Stack, M.S., and Friedl, P. (2007). Multi-step pericellular proteolysis controls the transition from individual to collective cancer cell invasion. Nat. Cell Biol. *9*, 893–904. https://doi.org/10.1038/ncb1616.

22. Gaggioli, C., Hooper, S., Hidalgo-Carcedo, C., Grosse, R., Marshall, J.F., Harrington, K., and Sahai, E. (2007). Fibroblast-led collective invasion of carcinoma cells with differing roles for RhoGTPases in leading and following cells. Nat. Cell Biol. *9*, 1392–1400. https://doi.org/10.1038/ncb1658.

23. Rappel, W.-J., Nicol, A., Sarkissian, A., Levine, H., and Loomis, W.F. (1999). Self-organized Vortex State in Two-Dimensional Dictyostelium Dynamics. Phys. Rev. Lett. *83*, 1247–1250. https://doi.org/10.1103/PhysRevLett.83.1247.

24. Zhang, J., Goliwas, K.F., Wang, W., Taufalele, P.V., Bordeleau, F., and Reinhart-King, C.A. (2019). Energetic regulation of coordinated leader–follower dynamics during collective invasion of breast cancer cells. Proc. Natl. Acad. Sci. USA *116*, 7867–7872. https://doi.org/10.1073/pnas.1809964116.

25. Ilina, O., Gritsenko, P.G., Syga, S., Lippoldt, J., La Porta, C.A.M., Chepizhko, O., Grosser, S., Vullings, M., Bakker, G.-J., Starruß, J., et al. (2020). Cell–cell adhesion and 3D matrix confinement determine jamming transitions in breast cancer invasion. Nat. Cell Biol. *22*, 1103–1115. https://doi.org/10.1038/s41556-020-0552-6.

26. Hiraki, H.L., Matera, D.L., Wang, W.Y., Prabhu, E.S., Zhang, Z., Midekssa, F., Argento, A.E., Buschhaus, J.M., Humphries, B.A., Luker, G.D., et al. (2023). Fiber density and matrix stiffness modulate distinct cell migration modes in a 3D stroma mimetic composite hydrogel. Acta Biomater. *163*, 378–391. https://doi.org/10.1016/j.actbio.2022.09.043.

27. Chaudhuri, O., Koshy, S.T., Branco da Cunha, C., Shin, J.-W., Verbeke, C.S., Allison, K.H., and Mooney, D.J. (2014). Extracellular matrix stiffness and composition jointly regulate the induction of malignant phenotypes in mammary epithelium. Nat. Mater. *13*, 970–978. https://doi.org/10.1038/nmat4009.

28. Carey, S.P., Martin, K.E., and Reinhart-King, C.A. (2017). Three-dimensional collagen matrix induces a mechanosensitive invasive epithelial phenotype. Sci. Rep. *7*, 42088. https://doi.org/10.1038/srep42088.

29. Simon, T., and Bromberg, J.S. (2017). Regulation of the Immune System by Laminins. Trends Immunol. *38*, 858–871. https://doi.org/10.1016/j.it.2017.06.002.

30. Graner, F., and Glazier, J.A. (1992). Simulation of biological cell sorting using a two-dimensional extended Potts model. Phys. Rev. Lett. *69*, 2013–2016. https://doi.org/10.1103/PhysRevLett.69.2013.

31. Glazier, J.A., and Graner, F. (1993). Simulation of the differential adhesion driven rearrangement of biological cells. Phys. Rev. E Stat. Phys. Plasmas Fluids Relat. Interdiscip. Topics *47*, 2128–2154. https://doi.org/10.1103/physreve.47.2128.

32. Leineweber, W.D., and Fraley, S.I. (2023). Adhesion tunes speed and persistence by coordinating protrusions and extracellular matrix remodeling. Dev. Cell *58*, 1414–1428.e4. https://doi.org/10.1016/j.devcel.2023.05.013.

33. Packard, B.Z., Artym, V.V., Komoriya, A., and Yamada, K.M. (2009). Direct visualization of protease activity on cells migrating in three-dimensions. Matrix Biol. *28*, 3–10. https://doi.org/10.1016/j.matbio.2008.10.001.

Please cite this article in press as: Ranamukhaarachchi et al., Global versus local matrix remodeling drives rotational versus invasive collective migration of epithelial cells, Developmental Cell (2024), https://doi.org/10.1016/j.devcel.2024.11.021

34. Ferrari, R., Martin, G., Tagit, O., Guichard, A., Cambi, A., Voituriez, R., Vassilopoulos, S., and Chavrier, P. (2019). MT1-MMP directs force-producing proteolytic contacts that drive tumor cell invasion. Nat. Commun. *10*, 4886. https://doi.org/10.1038/s41467-019-12930-y.

35. Hotary, K., Allen, E., Punturieri, A., Yana, I., and Weiss, S.J. (2000). Regulation of cell invasion and morphogenesis in a three-dimensional type I collagen matrix by membrane-type matrix metalloproteinases 1, 2, and 3. J. Cell Biol. *149*, 1309–1323. https://doi.org/10.1083/jcb.149.6.1309.

36. Grafinger, O.R., Gorshtein, G., Stirling, T., Geddes-McAlister, J., and Coppolino, M.G. (2021). Inhibition of β1 integrin induces its association with MT1-MMP and decreases MT1-MMP internalization and cellular invasiveness. Cell. Signal. *83*, 109984. https://doi.org/10.1016/j.cellsig.2021.109984.

37. Grafinger, O.R., Gorshtein, G., Stirling, T., Brasher, M.I., and Coppolino, M.G. (2020). β1 integrin-mediated signaling regulates MT1-MMP phosphorylation to promote tumor cell invasion. J. Cell Sci. *133*, jcs239152. https://doi.org/10.1242/jcs.239152.

38. Soslau, G., Mason, C., Lynch, S., Benjamin, J., Ashak, D., Prakash, J.M., Moore, A., Bagsiyao, P., Albert, T., Mathew, L.M., et al. (2014). Intracellular matrix metalloproteinase-2 (MMP-2) regulates human platelet activation via hydrolysis of talin. Thromb. Haemost. *111*, 140–153. https://doi.org/10.1160/TH13-03-0248.

39. Golubkov, V.S., Boyd, S., Savinov, A.Y., Chekanov, A.V., Osterman, A.L., Remacle, A., Rozanov, D.V., Doxsey, S.J., and Strongin, A.Y. (2005). Membrane type-1 matrix metalloproteinase (MT1-MMP) exhibits an important intracellular cleavage function and causes chromosome instability. J. Biol. Chem. *280*, 25079–25086. https://doi.org/10.1074/jbc.M502779200.

40. Sung, M.M., Schulz, C.G., Wang, W., Sawicki, G., Bautista-López, N.L., and Schulz, R. (2007). Matrix metalloproteinase-2 degrades the cytoskeletal protein alpha-actinin in peroxynitrite mediated myocardial injury. J. Mol. Cell. Cardiol. *43*, 429–436. https://doi.org/10.1016/j.yjmcc.2007.07.055.

41. Jobin, P.G., Butler, G.S., and Overall, C.M. (2017). New intracellular activities of matrix metalloproteinases shine in the moonlight. Biochim. Biophys. Acta Mol. Cell Res. *1864*, 2043–2055. https://doi.org/10.1016/j.bbamcr.2017.05.013.

42. Levental, K.R., Yu, H., Kass, L., Lakins, J.N., Egeblad, M., Erler, J.T., Fong, S.F.T., Csiszar, K., Giaccia, A., Weninger, W., et al. (2009). Matrix crosslinking forces tumor progression by enhancing integrin signaling. Cell *139*, 891–906. https://doi.org/10.1016/j.cell.2009.10.027.

43. Mori, H., Lo, A.T., Inman, J.L., Alcaraz, J., Ghajar, C.M., Mott, J.D., Nelson, C.M., Chen, C.S., Zhang, H., Bascom, J.L., et al. (2013). Transmembrane/cytoplasmic, rather than catalytic, domains of Mmp14 signal to MAPK activation and mammary branching morphogenesis via binding to integrin β1. Development *140*, 343–352. https://doi.org/10.1242/dev.084236.

44. Wiseman, B.S., Sternlicht, M.D., Lund, L.R., Alexander, C.M., Mott, J., Bissell, M.J., Soloway, P., Itohara, S., and Werb, Z. (2003). Site-specific inductive and inhibitory activities of MMP-2 and MMP-3 orchestrate mammary gland branching morphogenesis. J. Cell Biol. *162*, 1123–1133. https://doi.org/10.1083/jcb.200302090.

45. Liu, X., Wu, H., Byrne, M., Jeffrey, J., Krane, S., and Jaenisch, R. (1995). A targeted mutation at the known collagenase cleavage site in mouse type I collagen impairs tissue remodeling. J. Cell Biol. *130*, 227–237. https://doi.org/10.1083/jcb.130.1.227.

46. Provenzano, P.P., Eliceiri, K.W., Campbell, J.M., Inman, D.R., White, J.G., and Keely, P.J. (2006). Collagen reorganization at the tumor-stromal interface facilitates local invasion. BMC Med. *4*, 38. https://doi.org/10.1186/1741-7015-4-38.

47. Fuhrmann, A., Banisadr, A., Beri, P., Tlsty, T.D., and Engler, A.J. (2017). Metastatic State of Cancer Cells May Be Indicated by Adhesion Strength. Biophys. J. *112*, 736–745. https://doi.org/10.1016/j.bpj.2016.12.038.

48. Gudjonsson, T., Rønnov-Jessen, L., Villadsen, R., Rank, F., Bissell, M.J., and Petersen, O.W. (2002). Normal and tumor-derived myoepithelial cells differ in their ability to interact with luminal breast epithelial cells for polarity and basement membrane deposition. J. Cell Sci. *115*, 39–50. https://doi.org/10.1242/jcs.115.1.39.

49. Rakha, E.A., Gandhi, N., Climent, F., van Deurzen, C.H.M., Haider, S.A., Dunk, L., Lee, A.H.S., Macmillan, D., and Ellis, I.O. (2011). Encapsulated papillary carcinoma of the breast: an invasive tumor with excellent prognosis. Am. J. Surg. Pathol. *35*, 1093–1103. https://doi.org/10.1097/PAS.0b013e31821b3f65.

50. Ahmed, K.M. (2017). Three-Dimensional Culture. In Encyclopedia of Cancer, M. Schwab, ed. (Springer), pp. 4511–4518. https://doi.org/10.1007/978-3-662-46875-3_7138.

51. Chin, A.S., Worley, K.E., Ray, P., Kaur, G., Fan, J., and Wan, L.Q. (2018). Epithelial Cell Chirality Revealed by Three-Dimensional Spontaneous Rotation. Proc. Natl. Acad. Sci. USA *115*, 12188–12193. https://doi.org/10.1073/pnas.1805932115.

52. Wu, P.-H., Giri, A., Sun, S.X., and Wirtz, D. (2014). Three-dimensional cell migration does not follow a random walk. Proc. Natl. Acad. Sci. U. S. A. *111*, 3949–3954. https://doi.org/10.1073/pnas.1318967111.

53. Wyckoff, J.B., Pinner, S.E., Gschmeissner, S., Condeelis, J.S., and Sahai, E. (2006). ROCK- and myosin-dependent matrix deformation enables protease-independent tumor-cell invasion in vivo. Curr. Biol. *16*, 1515–1523. https://doi.org/10.1016/j.cub.2006.05.065.

54. Hall, M.S., Alisafaei, F., Ban, E., Feng, X., Hui, C.-Y., Shenoy, V.B., and Wu, M. (2016). Fibrous nonlinear elasticity enables positive mechanical feedback between cells and ECMs. Proc. Natl. Acad. Sci. USA *113*, 14043–14048. https://doi.org/10.1073/pnas.1613058113.

Please cite this article in press as: Ranamukhaarachchi et al., Global versus local matrix remodeling drives rotational versus invasive collective migration of epithelial cells, Developmental Cell (2024), https://doi.org/10.1016/j.devcel.2024.11.021

CellPress
OPEN ACCESS

STAR★METHODS

KEY RESOURCES TABLE

REAGENT or RESOURCE	SOURCE	IDENTIFIER
Antibodies		
Alexa Fluor® Plus 405 Phalloidin	Invitrogen	A30104
Alexa Fluor® 488 Phalloidin	Cell Signaling Technologies	8878S
Alexa Fluor® Plus 647 Phalloidin	Invitrogen	A30107
Alexa Fluor® 647 Phalloidin	Invitrogen	A22287
Anti-rabbit IgG (H+L), F(ab')2 Fragment (Alexa Fluor® 488 Conjugate)	Cell Signaling Technologies	4412S; RRID: AB_1904025
Anti-mouse IgG (H+L), F(ab')2 Fragment (Alexa Fluor® 594 Conjugate)	Cell Signaling Technologies	8890S; RRID: AB_2714182
Anti-rabbit IgG, HRP-linked Antibody	Cell Signaling Technologies	7074; RRID: AB_2099233
Anti-mouse IgG, HRP-linked antibody	Cell Signaling Technologies	7076; RRID: AB_330924
Goat anti-Mouse IgG (H+L) Cross-Adsorbed Secondary Antibody, Alexa Fluor® 546	Invitrogen	A11003; RRID: AB_2534071
Goat anti-Rabbit IgG (H+L) Highly Cross-Adsorbed Secondary Antibody, Alexa Fluor® 546	Invitrogen	A11035; RRID: AB_2534093
Goat anti-Rabbit IgG (H+L) Highly Cross-Adsorbed Secondary Antibody, Alexa Fluor® 647	Invitrogen	A21245; RRID: AB_2535813
Mouse monoclonal Anti-Talin 1 and 2 antibody [8D4]	Abcam	Ab11188; RRID: AB_297828
Rabbit polyclonal Anti-α-actinin	Cell Signaling Technologies	3134; RRID: AB_2223798
Rabbit monoclonal Anti-GAPDH [14C10]	Cell Signaling Technologies	2118; RRID: AB_561053
Rabbit polyclonal Anti-Pericentrin	Sigma-Aldrich	ABT59; RRID: AB_10947564
Rabbit monoclonal anti-MMP-14 [EP1264Y]	Abcam	ab51074; RRID: AB_881234
Rabbit polyclonal Anti-Collagen Type 1 (3/4 fragment)	Adipogen	AG-25T-0116-C025; RRID: AB_3668951
Rabbit polyclonal Anti-Integrin β1	Cell Signaling Technologies	4706; RRID: AB_823544
Mouse monoclonal PE Anti-human CD29 Antibody [TS2/16]	Biolegend	303003; RRID: AB_314319
Mouse monoclonal Anti-Laminin-5, γ2 chain [D4B5]	Sigma-Aldrich	MAB19562; RRID: AB_94454
Rabbit monoclonal Anti-Pan-Cadherin [EPR1792Y]	Abcam	ab51034; RRID: AB_868609
Mouse monoclonal anti-E-cadherin [SHE78-7]	Invitrogen	13-5700; RRID: AB_2533022
Bacterial and Virus Strains		
DH5α chemically competent cells	Thermo Fisher	Cat#18258012
Chemicals, Peptides, and Recombinant Proteins		
DMEM, high glucose, pyruvate	Gibco	11995065
Fetal Bovine Serum	Corning	MT35010CV
Gentamicin	Thermo Fisher Scientific	15750060
DMEM/F12	Invitrogen	11330032
Horse Serum	Invitrogen	16050-122
Animal-Free Recombinant Human EGF	Peprotech	AF-100-15
Hydrocortisone	Sigma-Aldrich	H0888
Cholera Toxin, *Vibrio cholerae*, Type Inaba 569B, Azide Free	Sigma-Aldrich	227036
Insulin from bovine pancreas	Sigma-Aldrich	I1882
Polybrene	Sigma-Aldrich	TR-1003-G
DMSO	Sigma-Aldrich	D2650
Marimastat	Abcam	ab141276

(*Continued on next page*)

Please cite this article in press as: Ranamukhaarachchi et al., Global versus local matrix remodeling drives rotational versus invasive collective migration of epithelial cells, Developmental Cell (2024), https://doi.org/10.1016/j.devcel.2024.11.021

Continued

REAGENT or RESOURCE	SOURCE	IDENTIFIER
DAPI	Thermo Fisher Scientific	62248
Collagen I	Corning	CB354249
DQ Collagen I	Invitrogen	D12060
HI-FBS	Gibco	A3840001
Paraformaldehyde Aqueous Solution	Electron Microscopy Services	15710-S
Bovine Serum Albumin (BSA)	Sigma-Aldrich	A3858-50g
Blue fluorescent 1μm polystyrene microsphere	Invitrogen	F13080
PBS, pH 7.4	Thermo Fisher Scientific	10010023
Collagenase	Sigma-Aldrich	C0130
Halt Protease and Phosphatase Inhibitor Cocktail (100X)	Thermo Fisher Scientific	78440
RIPA Lysis and Extraction Buffer	Thermo Fisher Scientific	89900
Pierce Micro BCA Protein Assay Kit	Thermo Fisher Scientific	23235
4x Bolt LDS Sample Buffer	Invitrogen	B0007
NuPAGE Sample Reducing Agent (10X)	Invitrogen	NP0009
Clarity Western ECL Substrate	Bio-Rad	1705061
Critical Commercial Assays		
Lipofectamine 3000	Thermo Fisher	L3000008
BD Influx	BD	UC San Diego Human Embryonic Stem Cell Core Facility (hESCCF)
Nikon TiE inverted microscope	Nikon	MEA53100
Leica TCS SP8 inverted confocal microscope	Leica	UC San Diego School of Medicine Microscopy Core
Experimental Models: Cell Lines		
MDA-MB-231	ATCC	HTB-26
Lenti-X 293T	Takara	632180
SK-HEP-1	ATCC	HTB-52
MCF-10A	ATCC	CRL-10317
Recombinant DNA		
pHIV-H2BmRFP	Addgene	RRID: Addgene_18982
Dendra2-Lifeact-7	Addgene	RRID: Addgene_54694
mCherry-LifeAct-7	Addgene	RRID: Addgene_54491
psPAX2	Addgene	RRID: Addgene_12260
pMD2.G	Addgene	RRID: Addgene_12259
lentiCRISPR v2	Addgene	RRID: Addgene_52961
Software and Algorithms		
Fiji/ImageJ 2	NIH	RRID:SCR_002285
MATLAB R2022a	Mathworks, Inc.	RRID:SCR_001622
Metamorph	Molecular Devices	RRID:SCR_002368
NIS-Elements	Nikon	RRID:SCR_014329
Prism 9	Graphpad	RRID:SCR_002798
Bitplane Imaris	Oxford Instruments	RRID:SCR_007370
Cell trajectory and random walk analysis	Wu et al.[52]	https://doi.org/10.1073/pnas.1318967111
Cellular Potts Model	https://github.com/Rappel-lab/Potts_model_2023	ZENODO https://doi.org/10.5281/zenodo.13346008

EXPERIMENTAL MODEL AND SUBJECT DETAILS

Cell culture and cell transfection

MDA-MB-231 triple negative breast cancer cells were purchased from ATCC and SK-HEP-1 hepatocellular carcinoma cells were provided by Jason Sicklick at UC San Diego. All MDA-MB-231 and SK-HEP-1 cell lines were cultured in high glucose Dubecco's

Please cite this article in press as: Ranamukhaarachchi et al., Global versus local matrix remodeling drives rotational versus invasive collective migration of epithelial cells, Developmental Cell (2024), https://doi.org/10.1016/j.devcel.2024.11.021

CellPress
OPEN ACCESS

modified Eagle's medium (DMEM, Gibco), supplemented with 10% fetal bovine serum (FBS, Corning) and 0.1% gentamicin (Thermo Fisher Scientific). MCF-10A breast epithelial cells (ATCC) were maintained in DMEM/F12 medium (Invitrogen) supplemented with 5% horse serum (Invitrogen), 20 ng/mL epidermal growth factor (Peprotech), 0.5 μg/mL hydrocortisone (Sigma-Aldrich), 100 ng/mL cholera toxin (Sigma-Aldrich), 10 μg/mL insulin (Sigma-Aldrich), and 0.1% gentamicin (Thermo Fisher Scientific). All cell lines were maintained at 37°C and 5% CO_2 in a humidified environment.

To generate cells that express H2B-mCherry (pHIV-H2BmRFP, Addgene #18982), LifeAct-GFP (Dendra2-Lifeact-7, Addgene #54694) and mCherry-LifeAct (mCherry-LifeAct-7, Addgene #54491), we generated viral particles by transfecting plasmids into lentiX 293T cells (Clontech) along with the psPAX2 packaging vector (Addgene #12260) and the pMD2.G envelope vector (Addgene #12259). Viral particles were collected by removing culture medium 24 and 48 hours after transfection and filtering through a 0.45 μm filter. Transduced cells were treated with 10 μg/mL Polybrene reagent (Sigma-Aldrich) and a titration of viral particles for 24 hours. Fluorescent cells with the appropriate expression levels of H2B-mCherry, LifeAct-GFP and mCherry-LifeAct were expanded for FACS sorting. For positive selection via FACS, cells were centrifuged at 1400 rpm for 4 minutes before resuspending in FACS buffer (1% BSA, 0.5 mM EDTA in PBS). Samples were sorted at the stem cell core of Sanford Consortium of Regenerative Medicine (La Jolla, CA) on a BD Influx cell sorter (BD Biosciences). Fluorescent samples were compared to unstained WT controls of each respective cell line.

METHOD DETAILS

Treatment with pharmacological inhibitors

Matrix metalloproteinases were inhibited using broad-spectrum MMP inhibitor Marimastat (Abcam) at a concentration of 1μM. As a vehicle control, cells were treated with 0.01% (v/v) dimethyl sulfoxide (DMSO, Sigma-Aldrich). Media supplemented with pharmacological inhibitors was refreshed daily.

CRISPR-Cas9 mediated gene suppression of ITGβ1

Genetic knockdown of ITGβ1 was performed as described previously.[15] In brief, small guide RNAs targeting the ITGβ1 gene were cloned into lentiCRISPR v2 plasmid (Addgene #52961) following instructions from Feng Zhang, the plasmid supplier. The sg_RNA sequences were obtained from the GECKO human library A, and were as followed: *ITGB1* sg_RNA1 (5′-TGCTGTGTGTTTGCT CAAAC-3′), *ITGB1* sg_RNA2 (5′-ATCTCCAGCAAAGTGAAACC-3′). For this study, we used the sg_RNA1. The lentiCRISPR v2 vectors containing the cloned sgRNA were verified by sequencing and were used to generate viral particles via transfection into lentiX293 T cells (Clonetech) along with packaging expressing plasmid (psPAX2, Addgene #12260) and envelope expressing plasmid (pMD2.G, Addgene #12259). After 48h of transfection, viral particles were collected and purified by filtering with a 0.45 μm filter. MDA-MB-231 cells were transduced with viral particles and polybrene. Following overnight incubation, media was changed and cells were left in normal growth media (DMEM supplemented with 10% FBS and 0.1% gentamicin) for 24-48h. Subsequently, media was changed to selection media containing 2.5 μg/mL puromycin for at least 7d.

To select for knockout cells, MDA-MB-231 ITGβ1 sg_RNA1 cells were expanded in a tissue culture to ~80% confluency and harvested. Cells were centrifuged at 350xg and 4°C for 5 minutes before resuspending in 2% HI-FBS in PBS. Cells were incubated for 20 minutes at 4°C with PE anti-human CD-29, followed by 2x 2% HI-FBS/PBS washes. Samples were sorted at the stem cell core of Sanford Consortium of Regenerative Medicine (La Jolla, CA) on a BD Influx cell sorter (BD Biosciences, Franklin Lakes, NJ) and gated using unstained negative and stained MDA WT positive controls.

3D culture in high density collagen I matrices

Cells suspended in culture medium were embedded in 3D collagen I matrices by mixing with 10x reconstitution buffer (1:1 v/v) and high concentration, rat tail acid extracted type I collagen (Corning) to a final collagen I concentration of 6 mg/mL and final seeding density of 100,000 cells/mL. The pH was adjusted using 1 N sodium hydroxide, and the mixture was added to 48-well culture plates at a final volume of 200 μL. The mixture was polymerized by incubating at 37°C for 30 min, and an equal volume of culture media was added to the top of the gels. For labeling of remodeled collagen, dye-quenched (DQ) collagen type I (Thermo Fisher Scientific) was mixed into collagen hydrogels at a final working concentration of 100 μg/mL, prior to pH neutralization and gel polymerization. For WT 7 day phenotype studies, media was replenished every other day. For 7 day phenotype studies using pharmacological inhibitors, media was replenished every day.

7 day phenotype structure quantification

Following 7 days in 3D culture, cell structures were imaged at 10x magnification using a Nikon Ti-Eclipse Epifluorescent Inverted Microscope. For each biological replicate (n=3), three fields of view (FOV) were selected and z-stacks from the bottom to the top of the collagen gel (50 μm step-size) were taken under brightfield illumination. Images were exported as.tif files and opened in ImageJ (NIH) for analysis. Structures that were at least 100 μm away from the top and bottom of the gel were selected, manually traced using the "Freehand selections" tool, and their circularity was determined using the "Shape descriptors" measurement output. For each FOV, a minimum of 25 structures were traced. A circularity threshold of <0.6 and >0.8 was set to define ductal-like phenotypes and acinus-like phenotypes, respectively.

Please cite this article in press as: Ranamukhaarachchi et al., Global versus local matrix remodeling drives rotational versus invasive collective migration of epithelial cells, Developmental Cell (2024), https://doi.org/10.1016/j.devcel.2024.11.021

For long-term phenotype tracking, collagen gels were prepared in triplicate as described above. After 2 days in culture, cell structures were imaged at 10x magnification using a Nikon Ti-Eclipse Epifluorescent Inverted Microscope. Five fields of view (FOV) at least 100 μm away from the top and bottom were selected across the three biological replicates. The same FOVs were imaged daily until 7 days after seeding. Structures were manually traced and their circularity was determined in ImageJ (NIH), as described above.

Immunofluorescence staining

Cells embedded in 3D collagen I matrices were washed twice with 1x phosphate buffered saline (PBS, Gibco) briefly and fixed with 4% paraformaldehyde (Electron Microscopy Services) diluted in 1x PBS for 30 min at room temperature. Prior to fixation, the collagen gels were washed three times with 1x PBS for 5 min each, followed by three, 5 min rinses with 100 mM glycine solution prepared in 1x PBS. Subsequently, the collagen gels were scooped, transferred to 24-well culture plates and blocked overnight at 4°C with a 1x PBS solution containing 1% w/v bovine serum albumin (BSA, Sigma-Aldrich), 2.5% v/v goat serum, 2.5% v/v FBS (Corning), and varying concentrations of Triton-X-100 (0.02-0.2% v/v, Thermo Fisher Scientific). After blocking, gels were three times with 1x PBS for 5 min. Primary antibody was diluted in antibody dilution buffer, which is composed of 1x PBS with 1% w/v BSA (Sigma Aldrich), 2.5% v/v goat serum, 2.5% v/v FBS (Corning), and 0.02% v/v Triton-X-100 (Thermo Fisher Scientific). Collagen hydrogels were covered with diluted primary antibodies and incubated for 2 days at 4°C. Following primary antibody incubation, gels were washed three times with 1x PBS, 15 min each. Subsequently, hydrogels were incubated with diluted secondary antibodies for 1 day at 4°C. After secondary antibody labeling, the gels were washed three times with 1x PBS, 15 min each. For F-actin visualization, gels were incubated in phalloidin diluted in 1x PBS for 1-2 h at room temperature, protected from light with aluminum foil. Samples were washed with 1x PBS three times for 15 min each. To stain cell nuclei, DAPI (Thermo Fisher Scientific) was added for 10 min. All steps were done with constant agitation on an orbital shaker. Primary and secondary antibodies used for immunofluorescence staining are listed in the key resources table.

Biophysical gel 3D culture

MDA-MB-231 mCherry-LifeAct cells were suspended in culture medium (WT - complete DMEM, Vehicle - 0.01% DMSO in complete DMEM, MMPi - 1 μM Marimastat in complete DMEM) and were mixed 1:1 v/v with 1x reconstitution buffer to achieve a final concentration of 100,000 cells/mL. Next, 1 μm diameter, blue carboxylated microspheres (Thermo Fisher Scientific) were added to the cell-buffer mixture at a final concentration 1:50 (v/v) of the final gel volume (200 μL). Dye-quenched (DQ) collagen type I (Thermo Fisher Scientific) was added to the cell-buffer solution at a final working concentration of 100 μg/mL. Lastly, the cell-buffer solution was mixed into high concentration, rat tail acid extracted type I collagen (Corning) to reach the desired final collagen concentration of 6 mg/mL. Subsequently, the pH was adjusted to 7.0 using 1 N sodium hydroxide and the cell-gel solution was added to custom made PDMS wells mounted on 35mm, glass bottom dishes (FluoroDish, World Precision Instruments) following thorough mixing. Collagen gels were polymerized at 37°C in a humidified incubator for at least 30 min prior to covering the gel with culture medium.

Biophysical imaging of cell-ECM interactions

After 33-39 hours in culture, cells were transferred to a Tokai Hit stage-top incubator on a Nikon Ti-Eclipse Epifluorescent Inverted Microscope. Multichannel z-stacks with an axial displacement of 37 μm (1 μm step size) were acquired every 2 minutes for 2 hours using an oil-immersion 40x objective (NA 1.5). For each time interval, z-stacks through the cell body were taken in three channels (blue, green, and red), to visualize the fluorescent beads, DQ collagen, and mCherry-LifeAct, respectively. The acquired images had dimensions of 1024 x 1022 pixels and were captured under 2x2 binning, resulting in a pixel size of 3.03 μm. Invasive and rotational cells at the ~2-4-cell stage whose primary axis of spreading was along the XY plane were selected for quantitation.

Biophysical imaging preprocessing

Maximum intensity projections (MIPs) of the z-stacks were generated for each time point to generate 2D time series for each channel of the cell selected for analysis. Biophysical imaging analysis multichannel z-stacks and MIPs were saved as.tif files and opened in ImageJ (NIH) for processing and analysis. Unless stated otherwise, image processing was done by performing background subtraction on multichannel z-stacks using a 40 pixel rolling ball algorithm followed by a 2 pixel median filter in ImageJ.

Quantification of protrusion dynamics

For cell protrusion dynamics analysis, protrusions were manually tracked in ImageJ using MIP time series of the mCherry-LifeAct expressing cells. In order to determine the time duration or protrusion lifetime, each protrusion was tracked frame-by-frame from initial protrusion extension to complete protrusion retraction. Protrusions longer than 2 μm were included in analysis and a protrusion was considered fully retracted when their length dropped below this threshold. The mean maximum protrusion length and time duration of the protrusion (ie. "protrusion lifetime") was calculated for each cell. The number of protrusions greater than 2 μm observed over the course of the 2 hr imaging period was used to determine the "protrusion rate". For cells that did not form any protrusions greater than 2 μm in length during imaging, the mean maximum protrusion length and protrusion lifetime were both zero.

Quantification of DQ matrix remodeling

In order to quantify the degree of collagen remodeling, multichannel z-stacks were first cropped to a 165μm x 165μm field of view binary masks of the cell body were first generated using Otsu's thresholding method. Next, the fluorescence intensity of a 5 μm band surrounding the cell was measured in the green DQ channel at each time frame for each slice of the z-stack. The total fluorescence intensity (integrated density) values were summed and divided by the total area of the band in order to get mean fluorescence

Please cite this article in press as: Ranamukhaarachchi et al., Global versus local matrix remodeling drives rotational versus invasive collective migration of epithelial cells, Developmental Cell (2024), https://doi.org/10.1016/j.devcel.2024.11.021

CellPress
OPEN ACCESS

intensity. This value was divided by the mean fluorescence intensity of the background to get the signal/ background ratio, referred to as DQ Intensity.

To determine the localization of matrix remodeling, z-stacks of the DQ and mCherry LifeAct channels at the first time point (t = 1/61) were processed and analyzed in ImageJ. First, pseudo-flat field correction was done on the DQ channel to correct for uneven illumination and the resulting image was cropped to a 165μm x 165μm field of view. Background subtraction on the cropped DQ channel z-stack was then performed using a 100 pixel rolling ball algorithm followed by a 2 pixel median filter. After processing, MIPs of the DQ channel were generated and then binarized by manual thresholding using the Otsu method in order to distinguish signal from background. Next, 1 μm bands along the cell perimeter were generated from MIPs of the mCherry LifeAct channel. Lastly, the percent of the band area covered by DQ signal was determined using the "Area Fraction" measurement in ImageJ. This measurement is referred to as the "Perimeter Remodeling (%)".

For quantifying matrix remodeling on confocal images, the phalloidin channel was used to define the cell body for each slice of the z-stack. For the confocal dataset, a 3 μm band was used due to reduced scattering of out-of-plane light. Quantification of DQ intensity was conducted as described above.

Quantification of cell contractility

Uncropped MIP images of the blue channel were used to visualize traction force bead dynamics in ImageJ. After template matching and slice alignment to correct for drift, the images were cropped to a 162.5μm x 162.5μm field of view. Bead tracking was done on cropped MIPs of the blue channel using the Mosaic plugin in ImageJ, as previously described.[13,32] The resulting table containing XY coordinates for each bead in the field of view for each timepoint was saved and analyzed using a custom MATLAB script that identifies beads that moved during time-lapse imaging. First, a filter was applied to only analyze the trajectories of beads that were tracked at all time points. After filtering, the displacement at each time point from the initial point was determined for each bead. In order to distinguish beads that were actively being pulled from those moving due to Brownian motion, a moving standard deviation approach was employed. The trajectories of beads not removed by filtering were measured resulting in the "mean instantaneous bead speed" and "mean maximum displacement". The "% movers" metric corresponds to the percent of total beads in the field of view that satisfy this criteria. Example bead displacement plots were generated by plotting the initial and final XY tracking coordinates of beads identified as movers.

Imaging for migrational tracking

MDA-MB-231 H2B-LifeAct, SK-HEP-1 H2B-LifeAct and MDA-MB-231 crITGβ1 H2B-LifeAct cells were embedded in a 200μL 6 mg/mL Collagen I gel with 100,000 cells in a glass bottom 48-well plate, polymerized for 30 min at 37°C, and 200μL of culture medium was added on top. Following 24 hours of culture, the plate was transferred to a microscope stage top incubator on a Nikon Ti-E inverted microscope and z-stacks with an axial displacement of 35 μm (1.5 μm stepsize) were acquired at 40x magnification every 1 hour for 18-24 hours. Invasive and rotational cells at the two-cell stage were selected for speed quantification and all dividing cells were excluded, as determined by the H2B-mCherry channel. Given the presence of dividing cells, we quantified 10 hours of consecutive frames for speed and cell persistence calculations. Migrational tracking was conducted within the Bitplane Imaris software. First, background subtraction was performed on both the LifeAct-GFP and H2B-mCherry channels by setting threshold values to 5 and 10, respectively, using the built-in image processing plugin. Nuclei tracking was conducted using the Imaris object tracking plugin. Center of mass for calculating angular velocities was determined by generating a reference frame using the surface rendering of the LifeAct-GFP channel. The positions of all tracked cells over time were then exported as Excel sheets and analyzed for speed and cell persistence ratios. Invasive speeds were automatically calculated by the Imaris software. Angular speeds for rotational cells were calculated from the XY coordinates of nuclei relative to the LifeAct center of mass.

Cell persistence ratio, modified from the previously described metric to describe both rectilinear and angular migration, can be represented as the following equation[18]:

$$\Sigma_0^{n\ =\ frame} \frac{1\ \textit{if vector in same direction as previous frame}, 0\ \textit{if direction changes}}{n}$$

We redefine the metric here to quantify the likelihood that a cell's angular or rectilinear velocity vector remained in the same direction between consecutive imaging frames over the course of the 10 hours that rectilinear or angular speeds were calculated. Briefly, for rotational migration, we quantified the proportion of time that cells migrated consistently in a clockwise (CW) or counterclockwise (CCW) radial direction such that a value of 0 indicated directionless, oscillatory motion and a value of 1 indicates CW/CCW motion without a change in direction. A similar rectilinear persistence ratio for invasive cells is quantified as the proportion of time cells migrated consistently without changing direction (<90° from previous direction), using the formula for calculating the angle between two rectilinear vectors: $cos(\theta) = \frac{v_i \cdot v_f}{|v_i||v_f|}$ where v_i and v_f represent the initial and final velocity vectors.

Confocal microscopy

Immunostained confocal images were acquired using a Leica SP8 inverted confocal microscope. The microscope was equipped with a 40x water immersion objective, unless indicated otherwise. Samples were excited at the appropriate excitation wavelength for the fluorophore(s) of interest.

Please cite this article in press as: Ranamukhaarachchi et al., Global versus local matrix remodeling drives rotational versus invasive collective migration of epithelial cells, Developmental Cell (2024), https://doi.org/10.1016/j.devcel.2024.11.021

Cellular Potts model simulations

The CPM relies on minimization of an energy term, the Hamiltonian (H), to model cell dynamics on a connected square lattice. Our Hamiltonian consists of four terms: contact energy, a cell size constraint, actin polarization, ECM confinement:

$$H = H_{contact} + H_{size} + H_{polarization} + H_{ECM\ confinement}$$

$$H_{contact} = \sum_{i,j\ neighbors} J_{\tau(\sigma_i),\tau(\sigma_j)}\left(1 - \delta_{\sigma_i,\sigma_j}\right)$$

$$H_{size} = \lambda_a\left(a(\sigma_{cell}) - A\right)^2$$

$$H_{polarization} = -\lambda_p P \cdot \sum_{i,j \epsilon \sigma_{cell}} r_{i,j}$$

$$H_{ECM\ confinement} = \lambda_{ECM} P \cdot \sum_{i,j \epsilon \sigma_{cell}} S_{i,j}$$

The coupling strength (J) of the contact energy term is dependent on the types ($\tau(\sigma)$) of interacting lattice sites, where Jc,c models cell-cell adhesion strength, Jc,e represents cell-ECM adhesion strength and Jc,m corresponds to cell-medium interfacial tension. The cell size constraint accounts for the energy cost for a cell to deviate from its optimal size, where A is the target cell area and $a(\sigma i)$ is the area of the cell with label i. The cell polarization vector (P) models polarization of the actin cytoskeleton, and is governed by:

$$\frac{dP_x}{dt} = k_+ \frac{v_x}{|v|}\left(1 - |P|\right) - k_- P_x$$

$$\frac{dP_y}{dt} = k_+ \frac{v_y}{|v|}\left(1 - |P|\right) - k_- P_y$$

These equations simulate the positive feedback between cell motion (v) and actin polarization dynamics, where a cell's orientation and propulsion intensity is dependent on rate of production (k+) and the rate of degradation (k-) of the polarization vector (P). We can also define the polarization persistence, $\gamma = k+/k-$, as the ratio between the two rates to determine how quickly the direction of the polarization vector is updated. To capture ECM remodeling, we incorporated the fact that remodeling can occur through both proteolytic cleavage and physical disruption.[5,22,53,54] Consistently, we incorporated a matrix-remodeling agent (E) that can be produced either locally or globally, given by:

$$\frac{dE}{dt} = D\nabla^2 E + k_g \delta_{\sigma_{i,j},\sigma_{cell}} + k_l \delta_{\sigma_{i,j},\sigma_{cell.tip}} - k_d E - k_r E S$$

$$\frac{dS}{dt} = -k_r E S$$

$$\sigma_{cell.tip} = \sigma_{cell} \cap \left[P_{i,j} \geq 0.99 \times max\left(\sum_{\forall i,j} r_{i,j} \cdot P\right)\right]$$

where D is the diffusion coefficient, δ is the kronecker delta, k_g and k_l are the respective rates of global and local agent production, k_d is the auto-degradation rate of the agent and kr is the reaction rate of the agent with the ECM. For local remodeling, each individual cell only releases the agent locally at the tip of the cell, as determined by the direction of the polarization vector (P) and only when the cell element is in contact with an ECM element. In the mode of global remodeling, the agent release is non-directional and over the whole cell body. We capture physical confinement by the ECM as an ECM penetration penalty where the penetration cost is proportional to the concentration of the ECM (S) and the parameter that indicates the strength of the ECM (λECM). Lastly, we simulated proliferation by modeling cell growth followed by division. Cells grow to a target size A(t) increased by the growth rate G(t) as a function of time. As the number of cells in a 2D cross-section actually corresponds to a larger number of cells in 3D, we incorporated a

Please cite this article in press as: Ranamukhaarachchi et al., Global versus local matrix remodeling drives rotational versus invasive collective migration of epithelial cells, Developmental Cell (2024), https://doi.org/10.1016/j.devcel.2024.11.021

CellPress
OPEN ACCESS

term, k >1, in our proliferation model to account for the differences between experiment and simulation. This simulated cell growth be summarized as:

$$\frac{dA(t)}{dt} = G(t) = \frac{G_0}{k^t}$$

We then employed a stochastic approach to model division such that when the cell area exceeds a threshold value (Athres = pA-max, with p equals 0.85 in our model), it divides into two smaller cells with a fixed probability at each simulation step.

The circularity in phase diagrams was calculated as 4*pi*area/perimeter^2, where the area and perimeter were determined from the bounding area that envelops the 2-cell cluster (using MATLAB alphaShape function). The angular velocity was calculated by finding the angular distance (angle, in radian) traveled by individual cells per unit time with respect to the center of mass of the cluster. The unit of the angular speed is radian per hour (rad/h).

Quantification of simulated protrusions

The simulated protrusion dynamic is quantified based on the polarization vector (P) of each cell. Specifically, we track the evolution of a polarization vector by recording its magnitude and direction. We assume that when the direction of the polarization vector deviates more than a certain threshold ($\Delta\theta = 2.5^\circ$), a new protrusion will form and the old protrusion will cease. Thus, the protrusion lifetime (τ) is calculated as the time elapsed between the formation and cessation of a protrusion. In addition, we can approximate the simulated protrusion length (l) to be the product of the polarization vector magnitude and the protrusion lifetime (i.e. $l = |P| \cdot \tau$ in arbitrary units). To mimic the incapability to experimentally measure protrusions that are too tiny, we define a length threshold (4 A.U.) and exclude these tiny protrusions from the protrusion population.

MMP-cleaved Collagen Quantification

MDA-MB-231 WT and MDA-MB-231 crITGβ1 cells were embedded in a 200μL 6mg/mL Collagen I gel at a seeding density of 50,000 cells and treated immediately with 0.01% DMSO (Vehicle) or 1uM Marimastat (MMPi) for 48h. Immunostained z-stack confocal images were acquired using a Leica SP8 inverted confocal microscope. Quantification of collagen $^3/_4$ R.F.U. was conducted as following in ImageJ. First, z-stack images were projected using the sum intensity method. Second, an ROI around signal region was drawn. Third, the sum of pixel intensity (integrated density) within a structure was measured. Fourth, the average background signal intensity was measured using an ROI of the same area to that of the signal region. Fifth, we normalized the pixel intensity within a structure to the background signal intensity using the following:

$$^3/_4\ Collagen\ Intensity = Integrated\ Density - (Area\ of\ Structure * Average\ Fluorescence\ of\ background)$$

Immunostaining Distribution Quantification

MDA-MB-231 WT and MDA-MB-231 crITGβ1 cells were embedded in a 200μL 6mg/mL Collagen I gel at a seeding density of 50,000 cells and treated immediately with 0.01% DMSO (Vehicle) or 1uM Marimastat (MMPi) for 48h. Immunostained z-stack confocal images were acquired using a Leica SP8 inverted confocal microscope equipped with a 40x oil immersion lens. Quantification of MT1-MMP signal distribution skewness was conducted as follows in ImageJ. First z-stacks of the MT1-MMP channel were duplicated and one of the stacks was processed using a gaussian blur (σ=2). MIPs of both z-stacks of the MT1-MMP channel were generated. The unprocessed MIP was binarized by thresholding using the Li method in order to create an along the perimeter of the collective cell structure. A 1μm band along this pericellular membrane was created and the skewness in the distribution of MT1-MMP signal within the band was measured using the "Skewness" measurement in ImageJ. For quantification of ITGβ1 signal distribution skewness, z-stacks of the channel were processed using a gaussian blur (σ=2) and a MIP of the processed channel was generated. The same 1μm band used to quantify MT1-MMP distribution along the pericellular membrane was used to measure the skewness in the distribution of ITGβ1 signal.

Western blot analysis

MDA-MB-231 WT and MDA-MB-231 crITGβ1 cells were embedded in a 400μL 6mg/mL rat tail acid extracted type collagen I gel at a seeding density of 500,000 cells/mL. Following neutralization with 1 N sodium hydroxide, the mixture was cast into a 24-well plate, and polymerized at 37°C for 30 min. Following polymerization, an equal volume of culture media was added to the top of the gel. After 24h and 48h in culture, the 3D collagen I gels were digested using 10 mg/mL collagenase (Sigma-Aldrich) at 37°C for 20 min, and filtered through a 35μm filter. After washing once with 1x PBS, cells were lysed using 200μL RIPA lysis buffer (Thermo Fisher Scientific) supplemented with 1x Halt Protease and Phosphatase Inhibitor Cocktail (Thermo Fisher Scientific). Cell lysates were kept on ice, vortexed every 5 min for a total of 30 min, and stored long-term at -20°C. Protein content was determined using a Pierce Micro BCA Protein Assay Kit (Thermo Fisher Scientific), according to the manufacturer's instructions. Samples were prepared by mixing 12-20μg of protein lysates with 4x Bolt LDS Sample Buffer (Invitrogen) and 10x NuPAGE Sample Reducing Agent (Invitrogen). Samples were then boiled at 95°C for 5 min and resolved on 10-12% SDS-PAGE gels with appropriate running buffer. Following gel electrophoresis, protein was transferred onto a 0.45μm PVDF membrane (Millipore) and blocked with 5% BSA in 1x TBST for 1h at RT. Membranes were then incubated overnight at 4°C with appropriate primary antibodies. Membranes were washed three times with 1x TBST for 5 min, and then incubated with the appropriate HRP-conjugated secondary antibody for 1h at room temperature. After washing three times with 1x TBST, the signal was developed by incubating the membranes in Clarity ECL Western Blotting Substrate (Biorad).

Please cite this article in press as: Ranamukhaarachchi et al., Global versus local matrix remodeling drives rotational versus invasive collective migration of epithelial cells, Developmental Cell (2024), https://doi.org/10.1016/j.devcel.2024.11.021

Densitometry quantification was performed using ImageJ software (NIH). Primary and secondary antibodies used for Western blotting are listed below.

QUANTIFICATION AND STATISTICAL ANALYSIS

Principal component analysis (PCA) and all statistical tests were performed using Graphpad Prism. PCA analysis of the biophysical imaging data was performed by z-normalizing the eight cell-ECM measurements for rotational and invasive cells analyzed in the wild-type dataset using the Graphpad Prism PCA tool. Student t-tests were used to perform the means of two populations. One-way ANOVA analyses followed by Tukey post-hoc tests for multiple comparisons were performed to compare the mean of three or more populations. Statistical significance is indicated as *, **, ***, **** for $p \leq 0.05$, $p \leq 0.01$, $p \leq 0.001$, $p \leq 0.0001$. See figure captions for the number of replicates analyzed.